Check for updates

*Advanced Materials*

ADVANCED MATERIALS
www.advmat.de

RESEARCH ARTICLE OPEN ACCESS

# Epitaxially Integrated Electro-Optic $KNbO_3$ Thin Films on Silicon

Sankalpa Hazra[1] | Tobias Schwaigert[2,3] | Yingxin Zhu[4] | Aiden Ross[1] | Muhammad Aminul Haque Chowdhury[1,5] | Shun-Li Shang[1] | Sameer Singh[6] | Zhiyu Zhang[4] | Zhe Wang[3] | Brynn Brower[6] | Saugata Sarker[1] | Suchismita Sarker[7] | Zi-Kui Liu[1] | Rama K. Vasudevan[8] | Long-Qing Chen[1] | Yang Yang[4] | Darrell G. Schlom[3,9,10] | Venkatraman Gopalan[1,6]

[1]Department of Materials Science and Engineering, The Pennsylvania State University, University Park, Pennsylvania, USA | [2]Platform For the Accelerated Realization, Analysis, and Discovery of Interface Materials (PARADIM), Cornell University, Ithaca, New York, USA | [3]Department of Materials Science and Engineering, Cornell University, Ithaca, New York, USA | [4]Department of Engineering Science and Mechanics, The Pennsylvania State University, University Park, Pennsylvania, USA | [5]Department of Electrical Engineering, The Pennsylvania State University, University Park, Pennsylvania, USA | [6]Department of Physics, The Pennsylvania State University, University Park, Pennsylvania, USA | [7]Cornell High Energy Synchrotron Source, Cornell University, Ithaca, New York, USA | [8]Center For Nanophase Materials Sciences, Oak Ridge National Laboratory, Oak Ridge, Tennessee, USA | [9]Kavli Institute at Cornell for Nanoscale Science, Ithaca, New York, USA | [10]Leibniz-Institut Für Kristallzüchtung, Berlin, Germany

**Correspondence:** Venkatraman Gopalan (vgopalan@psu.edu)

**Received:** 26 March 2026 | **Revised:** 1 September 2026 | **Accepted:** 11 September 2026

**Keywords:** epitaxy | ferroelectricity | materials science | optoelectronics | photonics | pockels effect | silicon | silicon photonics | thin film | transmission electron microscopy

## ABSTRACT

The absence of a native electro-optic effect in silicon remains a fundamental limitation for integrated photonics, motivating the integration of ferroelectric oxides as active materials. Here, we report the first epitaxial integration of $KNbO_3$ thin films on silicon, establishing a new materials platform for silicon-integrated electro-optics. Silicon integration of $KNbO_3$ has remained unexplored due to potassium volatility challenges during synthesis. Employing suboxide molecular-beam sources assisted by in situ RHEED monitoring and guided by thermodynamic simulations, we establish an adsorption-controlled growth window for phase-pure $KNbO_3$ films. Temperature dependent x-ray diffraction, optical second-harmonic generation, piezo-response force microscopy, and transmission electron microscopy aided by phase-field simulations confirm high-quality epitaxial films with sharp interfaces and structural phase transitions mirroring $KNbO_3$ single crystals. Electro-optic measurements demonstrate a linear Pockels response with an effective electro-optic response of 146 $\pm$ 14 pm $V^{-1}$ at 1550 nm. Phase-field simulations further predict that modest compressive strain can drive the electro-optic response to ~900 pm $V^{-1}$. Beyond $KNbO_3$, this integration pathway provides access to the broader $(K,Na)(Ta,Nb)O_3$ family, opening pathways to harness their strong electro-optic response, nonlinear optical response, piezoelectric response and ferroelectric properties for next-generation silicon photonics and electronics beyond current $BaTiO_3$-based approaches.

Sankalpa Hazra and Tobias Schwaigert contributed equally to this work.

This is an open access article under the terms of the Creative Commons Attribution License, which permits use, distribution and reproduction in any medium, provided the original work is properly cited.
© 2026 The Author(s). *Advanced Materials* published by Wiley-VCH GmbH

## 1 | Introduction

The integration of functional oxides with silicon has emerged as a critical pathway toward overcoming fundamental limitations in photonics and electronics [1, 2]. Silicon, despite its dominance in microelectronics and increasing role in photonics, lacks useful properties that are present in ferroelectrics such as the electro-optic effect. This constrains the development of key functionalities including efficient electro-optic modulation [3] and on-chip optical switching [4]. Ferroelectric perovskite oxides offer a solution by providing strong electro-optic effects and large spontaneous polarization. Integration of these oxides directly onto silicon substrates enables monolithic devices that leverage silicon's mature processing infrastructure, low cost, and CMOS compatibility while accessing the functional capabilities of complex oxides. The successful epitaxial integration of ferroelectric perovskites on silicon has validated this approach. $BaTiO_3$ has been demonstrated as a platform for electro-optic modulators in silicon photonics, exploiting its Pockels response [2].

Among oxide ferroelectrics, potassium niobate ($KNbO_3$) presents a compelling case for silicon integration. $KNbO_3$ possesses a polar-optic coefficient, $g_{1111}$, that is 50% larger [5] than that of $BaTiO_3$, reflecting a stronger intrinsic coupling between ferroelectric polarization and optical properties, and exhibits bulk electro-optic coefficients of $r_{42} = 450 \pm 30$ pm $V^{-1}$ [6]. A $T_c$ of 676 K [7] in bulk $KNbO_3$ provides a wide operational window over which its electro-optic performance can be sustained, exceeding that of bulk $BaTiO_3$ [8]. Additionally, $KNbO_3$ has superior transverse electrostrictive coefficient ($|Q_{13}| \approx 0.053\ m^4C^{-2}$) [8], significantly larger than that of $BaTiO_3$ ($|Q_{13}| \approx 0.034\ m^4C^{-2}$) [8, 9] and $PbTiO_3$ ($|Q_{13}| \approx 0.026\ m^4C^{-2}$) [8, 10], providing exceptionally strong coupling between strain and ferroelectric polarization. This strong strain-polarization coupling translates directly into enhanced piezoelectric coefficients [11], opening pathways toward high-performance piezo-optomechanical photonic transducers on silicon [12].

Beyond these intrinsic properties, $KNbO_3$ serves as the entry point to the $(K,Na)(Ta,Nb)O_3$ family on silicon, a compositional space whose functional potential for photonics and electronics remains largely unexplored. For example, $KNbO_3$ [8, 13] and $(K,Na)NbO_3$ [14, 15] are already known to produce large enhancements in nonlinear optical properties. Additionally, $K(Ta,Nb)O_3$ which is accessible through the same compositional space, exhibits a giant quadratic electro-optic response [16], enabling applications in beam steering and photorefractive devices inaccessible to conventional Pockels materials.

Despite these attributes, synthesis challenges arising from potassium volatility have limited efforts to integrate $KNbO_3$ on silicon substrates. Based on our recent demonstration of the epitaxial growth of $KNbO_3$ thin films by suboxide molecular-beam epitaxy (*S*-MBE) on rare-earth scandate substrates ($ReScO_3$, Re = Gd and Dy) [8], in this work we extend this epitaxial integration to silicon using a $SrTiO_3$ buffer layer. We employ transmission electron microscopy and synchrotron x-ray diffraction to characterize the crystallinity and epitaxial quality of the strain-relaxed $KNbO_3/SrTiO_3/Si$ heterostructures. Temperature-dependent optical second-harmonic generation, x-ray diffraction, and piezo-response force microscopy aided by phase-field simulations is used to probe phase transitions and domain structures. Finally, electro-optic measurements are performed to determine the room temperature electro-optic coefficient of $KNbO_3$ integrated on silicon. These results establish a viable pathway for incorporating this high-performance, lead-free ferroelectric into silicon photonic and electronic platforms.

### 1.1 | Growth of $KNbO_3$ Using Molecular-Beam Epitaxy

Aided by thermodynamic calculations, we systematically map the adsorption-controlled growth window of phase-pure $KNbO_3$ thin films on single-crystal $SrTiO_3$ substrates. This mapping provides clear guidance for the subsequent synthesis of $KNbO_3$ on silicon substrates upon which a 100 nm $SrTiO_3$ buffer layer is first deposited by MBE [17]. A thermodynamic framework (see Methods, Figure S1) was employed to evaluate the phase stability of potassium–niobium oxides as a function of potassium partial pressure and substrate temperature. These calculations are summarized in an Ellingham-type phase stability diagram (Figure 1a), constructed at a fixed oxygen partial pressure of $7.5 \times 10^{-4}$ Torr. This diagram serves as a practical guide for identifying regimes in which $KNbO_3$ is thermodynamically favored over competing phases.

To enable the growth of $KNbO_3$ thin films, several approaches have been developed to address the synthesis challenges associated with highly volatile alkali-containing oxides. One approach is the pulsed-laser deposition (PLD) scheme, in which $K_2O$ is thermally evaporated [18]. In such a scheme, the gas-phase species generated during $K_2O$ evaporation depend sensitively on the oxygen partial pressure, complicating quantitative control over the potassium chemical potential at the growth surface. In contrast, our approach relies on the direct evaporation of elemental potassium from an intermetallic $KIn_4$ source, for which the vapor pressure of potassium exceeds that of indium by approximately eleven orders of magnitude [19]. This enables a stable and well-defined potassium flux without introducing additional oxygen-dependent gas-phase equilibria. During growth, reflection high-energy electron diffraction (RHEED) was recorded continuously, providing real-time feedback on surface structure and phase evolution. Across the explored parameter space, multiple phases were observed. To directly probe phase stability and surface stoichiometry, we combine in situ RHEED with potassium partial pressures calculated from QCM-measured $K_2O$ fluxes immediately prior to each growth (see Supporting Information).

Figure 1a summarizes the experimentally accessible growth regimes at 675°C as a function of potassium partial pressure. While in theory the growth window extends to low overpressures of potassium over a substrate surface (Figure S1), the range of potassium overpressures no longer provide a reasonable film growth rate below $\sim 10^{-8}$ Torr. For example, a substrate temperature of 675°C and a potassium overpressure of $10^{-9}$ Torr corresponds to a potassium flux of $\sim 7 \times 10^{11}$ K atoms $cm^{-2}\ s^{-1}$, [20], which if it were all consumed to form $KNbO_3$ would yield a $KNbO_3$ growth rate of just 0.005 $Å s^{-1}$. To compare the theoretical overpressure of potassium needed to stabilize $KNbO_3$ to the



15214095, 2026, 63, Downloaded from https://advanced.onlinelibrary.wiley.com/doi/10.1002/adma.75067, Wiley Online Library on [16/11/2026]. See the Terms and Conditions (https://onlinelibrary.wiley.com/terms-and-conditions) on Wiley Online Library for rules of use; OA articles are governed by the applicable Creative Commons License

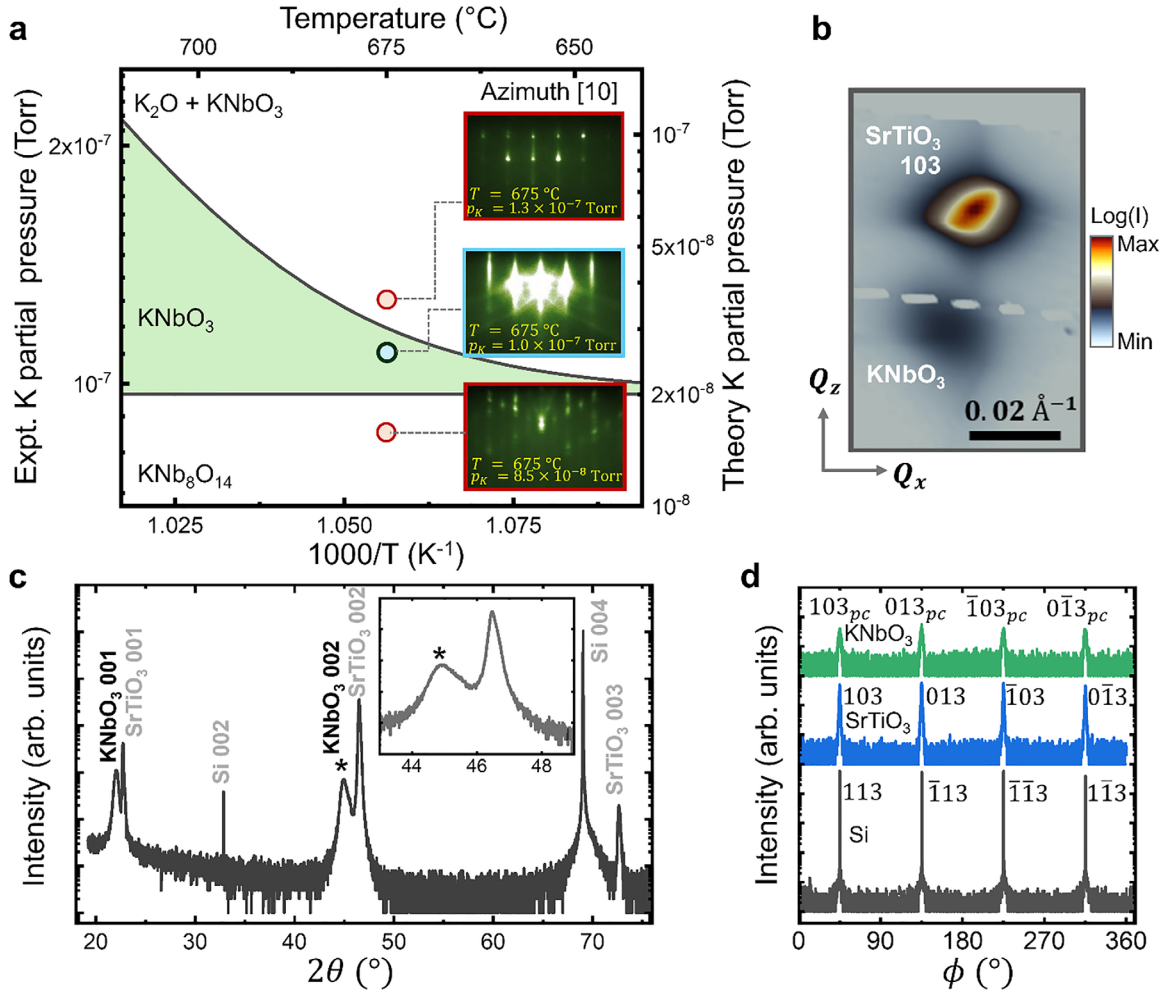



**FIGURE 1** | (a) Growth window for $KNbO_3$: Theoretically calculated potassium partial pressure (right axis) as a function of growth temperature showing predicted adsorption-controlled growth window for $KNbO_3$ (shaded region), bounded by potassium-rich ($K_2O$ + $KNbO_3$) and potassium-deficient ($KNb_8O_{14}$) phase conditions. Thermodynamically predicted potassium overpressures (Figure S1) are converted into potassium partial pressures required for the growth of $KNbO_3$ (right axis) by adding the potassium partial pressure consumed during $KNbO_3$ growth. Experimental potassium partial pressures, determined from QCM-calibrated fluxes prior to each deposition, are shown on the left axis. In situ RHEED patterns for different growth regimes are shown in insets. The blue inset represents best experimental growth conditions while the red insets represent the potassium-rich and potassium-deficient conditions. Although the left and right (theory/experiment) axes are in qualitative agreement regarding the location of the adsorption-controlled growth window for single-phase $KNbO_3$ (the green shaded region), quantitatively they do not precisely coincide. This is to be expected given the uncertainty of the thermodynamic parameters used and oxygen partial pressure. (b) Synchrotron XRD reciprocal space map around the 103 $SrTiO_3$ and $KNbO_3$ peaks. (c) Lab $\theta - 2\theta$ XRD scans showing only $00\ell$ peaks of Si, $SrTiO_3$, and $KNbO_3$. Inset shows zoom in around the 002 $KNbO_3$ peak. (d) Lab XRD $\phi$-scans around $KNbO_3$ $103_{pc}$, $SrTiO_3$ 103 and Si 113-type reflections.

experimental potassium partial pressures ($p_K$) used for the growth of $KNbO_3$, one would need to add the potassium partial pressure corresponding to the potassium flux that is being consumed to form $KNbO_3$ (which is equal to the niobium flux used for $KNbO_3$ growth) to the theoretically predicted potassium overpressures.

Experimentally, typical potassium fluxes used for growth range from ~6.0 $\times 10^{13}$ to 9.2 $\times$ $10^{13}$ atoms $cm^{-2}$ $s^{-1}$ with a Nb flux of ~1.5 $\times 10^{13}$ atoms $cm^{-2}$ $s^{-1}$. To better compare our thermodynamic calculations of the potassium overpressure conditions under which $KNbO_3$ is stable with the experimental conditions under which we have grown $KNbO_3$, we construct a theoretical potassium partial pressure axis in Figure 1a. In this axis, the partial pressure of potassium being consumed during growth is added to the overpressure needed according to our thermodynamic calculations. In our case, with a $NbO_2$ flux of ~$1.5 \times 10^{13}$ atoms $cm^{-2}$ $s^{-1}$, the flux of potassium being consumed during growth is also ~$1.5 \times 10^{13}$ atoms $cm^{-2}$ $s^{-1}$. The corresponding potassium partial pressure ~$2 \times 10^{-8}$ Torr then compares to the theoretical case of having no potassium overpressure.

Experimental potassium overpressures ($p_K$) achieved during growth are calculated to range from 8.5 $\times$ $10^{-8}$ Torr to 1.3 $\times$ $10^{-7}$ Torr corresponding to potassium fluxes ranging from 6.0 $\times 10^{13}$ to 9.2 $\times$ $10^{13}$ atoms $cm^{-2}$ $s^{-1}$. At high potassium overpressures (e.g., the potassium-rich condition, $p_K \approx 1.3 \times 10^{-7}$ Torr), a spotty RHEED pattern is observed, indicating higher surface roughness owing to excess potassium accumulation at the surface, consistent with the coexistence of $K_2O$ and $KNbO_3$ predicted



15214095, 2026, 63, Downloaded from https://advanced.onlinelibrary.wiley.com/doi/10.1002/adma.75067, Wiley Online Library on [16/11/2026]. See the Terms and Conditions (https://onlinelibrary.wiley.com/terms-and-conditions) on Wiley Online Library for rules of use; OA articles are governed by the applicable Creative Commons License

from thermodynamic calculations under potassium-rich conditions. In contrast, at an intermediate potassium overpressure of $p_K \approx 1.1 \times 10^{-7}$ Torr (ideal condition), sharp and well-defined streaky RHEED features are observed, characteristic of smooth, two-dimensional growth, and phase-pure $KNbO_3$. Reducing the potassium overpressure further to $p_K \approx 8.5 \times 10^{-8}$ Torr (a potassium deficient condition) results in a loss of streak intensity, increased diffuse scattering, and additional diffractions patterns signaling the onset of competing niobium-rich phases, consistent with thermodynamic predictions identifying the formation of $KNb_8O_{14}$.

Employing in situ RHEED monitoring assisted by thermodynamic simulations provides a roadmap that enables immediate correction of growth parameters. Deviations from the optimal growth window can be detected in real time and compensated by adjusting the potassium flux or substrate temperature, allowing the system to be steered back into the adsorption-controlled regime highlighted in Figure 1a. Additionally, using a similar growth strategy, layer-by-layer growth of $KNbO_3$ has previously been demonstrated on closely lattice-matched $ReScO_3$ substrates. When $KNbO_3$ is grown on $SrTiO_3$, however, which imposes a larger lattice mismatch (~2.7%) and exceeds the estimated critical thickness for strain relaxation (~11 – 12 nm), island growth can become energetically favored over layer-by-layer growth, potentially promoting a three-dimensional growth mode. With a real-time feedback loop established to assess the phase stability of $KNbO_3$ growth on $SrTiO_3$ single crystals, we next turn to the synthesis of $KNbO_3$ on $SrTiO_3$/Si. The synthesis of 100 nm $SrTiO_3$ (001) on Si (001) is reported elsewhere [17]. RHEED patterns of $KNbO_3$ on $SrTiO_3$/Si confirming phase-pure $KNbO_3$ growth is shown in Figure S2.

To calculate the lattice parameter and strain state of $KNbO_3$, synchrotron-based reciprocal space mapping (RSM) was performed around the $SrTiO_3$ 103 peak (Figure 1b). From the observed $KNbO_3$ $103_{pc}$ peak, the average in-plane and out-of-plane lattice parameters are found to be 3.99 ± 0.01 and 4.03 ± 0.01 Å, respectively (Subscript '*pc*' stands for pseudocubic). This closely matches the expected room temperature orthorhombic phase lattice parameters of single crystal $KNbO_3$ ($apc$ = 3.97 Å, $cpc$ = 4.03 Å) [21], implying the strain-relaxed nature of our films. Additionally, phase-field simulations (see Supporting Information) of a $KNbO_3$ thin film on $SrTiO_3$/Si under 0% misfit strain reveal average lattice parameters of $apc$ = 4.01 Å, $cpc$ = 4.02 Å at 300 K, consistent with our experimental measurements.

Lab x-ray diffraction measurements were performed on $KNbO_3$ on $SrTiO_3$/Si to confirm the crystallinity and epitaxial relationship between $KNbO_3$ film and the $SrTiO_3$ buffer layer. The $\theta - 2\theta$ x-ray diffraction scan shown in Figure 1c exhibits only reflections corresponding to $KNbO_3$ and the underlying $SrTiO_3$/Si heterostructure, with no detectable secondary phases, confirming phase-pure integration of $KNbO_3$ on silicon. Additionally, rocking curve measurements around the $KNbO_3$ 001 reflection reveal two components: a sharp central peak (FWHM = 0.0097°) superimposed on a broader component (FWHM = 0.7497°), reflecting mosaic spread of the film arising from threading dislocations and misoriented sub-domains formed due to strain relaxation (Figure S2).

The in-plane orientation relationship between the layers of the film and substrate was determined from off-specular $\phi$-scans of $KNbO_3$ $103_{pc}$, $SrTiO_3$ 103 and Si 113 reflections. As shown in Figure 1d, the epitaxial orientation relationship is $KNbO_3$ $[100]_{pc}$ || $SrTiO_3$ [100] || Si [110] confirming epitaxial growth of $KNbO_3$ on $SrTiO_3$/Si. The alignment between $SrTiO_3$ [100] and Si [110] confirms the well-known 45° rotation of the $SrTiO_3$ unit cell with respect to the silicon conventional unit cell arising from a better lattice parameter match of $SrTiO_3$ ($a_{[100]}$ = 3.905 Å) along the Si [110] direction ($a_{[110]}/2$ = 3.84 Å) [22]. The epitaxial strain-relaxed nature of the $KNbO_3$ thin film is further confirmed by large-area RSM maps along both $Q_x$ and $Q_y$ directions, which show corresponding $KNbO_3$ peaks aligned with every $SrTiO_3$ peak (Figure S3).

AFM reveals a RMS surface roughness of 1.47 nm for a 18 nm thick film and 6.83 nm for a 96 nm thick film across a 10 μm × 10 μm area (Figure S4). A larger surface roughness would contribute to larger optical losses through scattering in waveguide geometries and hence presents a challenge for silicon integration. Roughness of the starting $SrTiO_3$/Si base film (0.97 nm) and the strain relaxed nature of the $KNbO_3$ films can contribute to the surface roughness. In comparison, surface roughness of ~0.55 nm was previously measured in commensurately strained 22 nm thick $KNbO_3$ films on closely lattice-matched $GdScO_3$ single crystal substrates using the same growth method [8]. These low roughness values can be achieved on silicon through lattice parameter tuned buffer layers replacing $SrTiO_3$. For example, by varying the barium concentration of compositionally graded (Ba,Sr)$TiO_3$ [23, 24] buffer layers, the lattice parameter can be tuned to eliminate or reduce the mismatch between the $KNbO_3$ film and the buffer layer. Alternatively, compositionally graded $SrSn_xTi_{1-x}O_3$ or $SrGe_xTi_{1-x}O_3$ buffer layers can also be used to achieve a similar lattice parameter tuning [25, 26]. A closely lattice-matched buffer layer would enable thicker commensurately strained $KNbO_3$ thin films with surface roughness mimicking those of $KNbO_3$ on $GdScO_3$ films.

## 1.2 | Structural Characterization by Transmission Electron Microscopy

To visualize the interface quality and crystalline structure of our films, transmission electron microscopy measurements were performed on $KNbO_3$/$SrTiO_3$/Si heterostructures. Figure 2a shows cross-sectional high-angle annular dark-field (HAADF) images and corresponding elemental energy-dispersive x-ray (EDX) maps of an 18 nm thick $KNbO_3$ thin film grown on $SrTiO_3$/Si. More comprehensive HAADF-STEM and EDX datasets for the two crystallographic viewing directions are shown in Figures S5 and S6, corresponding to the $SrTiO_3$ [1$\bar{1}$0] and [010] projections, respectively. From the EDX maps, a $SiO_x$ region is visible between the silicon substrate and $SrTiO_3$ buffer layer; it is created due to silicon oxidation owing to the high MBE growth temperatures which increases oxygen diffusion across the $SrTiO_3$ layer [27]. The thickness of the $SiO_x$ layer depends on growth parameters such as temperature and oxygen pressure, with previous reports demonstrating that even complete conversion of the silicon layer to $SiO_x$ is possible under appropriate



15214095, 2026, 63, Downloaded from https://advanced.onlinelibrary.wiley.com/doi/10.1002/adma.75067, Wiley Online Library on [16/11/2026]. See the Terms and Conditions (https://onlinelibrary.wiley.com/terms-and-conditions) on Wiley Online Library for rules of use; OA articles are governed by the applicable Creative Commons License

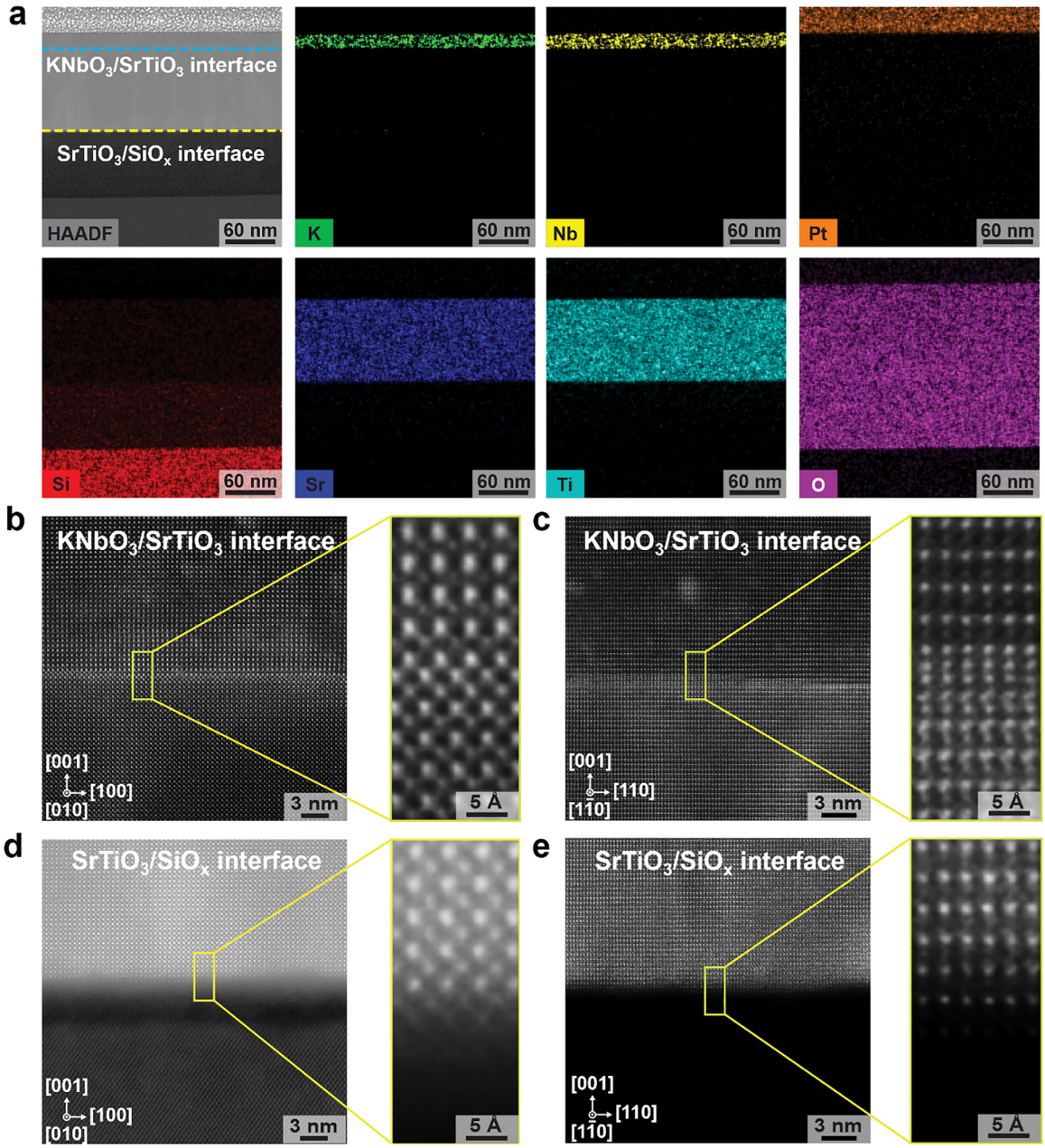



**FIGURE 2** | (a) Cross-sectional scanning transmission electron microscopy (STEM) high-angle annular dark-field (HAADF) image of the $KNbO_3/SrTiO_3/Si$ stack. The accompanying energy-dispersive x-ray spectroscopy (EDS) elemental maps (K, Nb, Sr, Ti, O, Si, and Pt) are acquired from the same field of view and illustrate the elemental distributions across the heterostructure. An amorphous $SiO_x$ interlayer is present between $SrTiO_3$ and the Si substrate. (b,c) Higher-magnification HAADF-STEM images of the $KNbO_3/SrTiO_3$ interface viewed along the $SrTiO_3$ [010] and [1$\bar{1}$0] zone axes, respectively. Insets show resolved atomic-column arrangements consistant with local epitaxial alignment across the $KNbO_3/SrTiO_3$ interface. (d,e) Higher-magnification HAADF-STEM images of the $SrTiO_3/SiO_x$ interface viewed along the $SrTiO_3$ [010] and [1$\bar{1}$0] zone axes, respectively, with corresponding atomic-resolution insets highlighting the transition from crystalline $SrTiO_3$ to the amorphous $SiO_x$ layer.

conditions [28]. Additionally, the high growth temperatures also promote silicon diffusion into the $SrTiO_3$ layer, as observed from the elemental maps, which can lead to amorphization of $SrTiO_3$ starting from the $SrTiO_3/SiO_x$ interface [29]. Silicon, however, does not penetrate the $KNbO_3$ layer. These signify the importance of using a sufficiently thick $SrTiO_3$ buffer layer for integration of oxide films on silicon. In this study, a ~100 nm thick $SrTiO_3$ buffer was used. The elemental maps otherwise reveal a sharp interface between the $KNbO_3$ film and $SrTiO_3$ buffer.

Figure 2b,c shows zoomed-in cross-sectional HAADF images from two different regions of the sample taken along the [010] and [1$\bar{1}$0] zone axes of $SrTiO_3$, respectively, revealing sharp, well-defined interfaces between $KNbO_3$ and $SrTiO_3$ in both regions. The resolved atomic-column arrangements supports a local epitaxial orientation relationship between $KNbO_3$ and $SrTiO_3$. In contrast, the interface between $SrTiO_3$ and $SiO_x$ exhibits a distinctly different structure (Figure 2d,e). An amorphous layer is observed in the immediate vicinity of the $SiO_x$ interface consistent with previous reports of strontium silicide formation [27] at



15214095, 2026, 63, Downloaded from https://advanced.onlinelibrary.wiley.com/doi/10.1002/adma.75067, Wiley Online Library on [16/11/2026]. See the Terms and Conditions (https://onlinelibrary.wiley.com/terms-and-conditions) on Wiley Online Library for rules of use; OA articles are governed by the applicable Creative Commons License

the interface between $SrTiO_3$ and $SiO_x$ as observed from EDX measurements (Figures S5 and S6). Additionally, $SrTiO_3$ can amorphize when grown on $SiO_x$ above 600°C [30, 31]. This amorphous layer, however, is confined only to the near-interface region, with the $SrTiO_3$ transitioning to a fully crystalline structure as the distance from the $SiO_x$ interface increases. This transition from amorphous to crystalline $SrTiO_3$ demonstrates that despite the interfacial disorder caused by silicon oxidation and the presence of $SiO_x$, the $SrTiO_3$ buffer layer successfully establishes high-quality crystalline growth that serves as an effective template for subsequent $KNbO_3$ epitaxy. The onset of the amorphous $SrTiO_3$ layer at the $SiO_x$ interface has previously been observed to occur at growth temperatures above 600°C, with the layer exceeding 100 nm in thickness for growth temperatures above 800°C, validating the necessity of a thick $SrTiO_3$ buffer layer [30].

Additionally, the TEM images reveal local atomic steps at the $KNbO_3/SrTiO_3$ interface (Figure 2c) and localized variations in atomic-column contrast near the interface and within the $SrTiO_3$ buffer layer (Figure S7). Because the imaged region represents a projection through the specimen thickness (~50 – 100 nm), atomic columns from different depths along the beam direction can overlap in projection, producing $KNbO_3$ – $SrTiO_3$ overlap patterns and apparent interfacial local distortion in the image. These distortions are hypothesized to arise from a combination of interfacial strain, which produces relative lattice offsets across the interface (Figures S8 and S9), and localized defects, such as threading dislocations and out-of-phase boundaries, in the $SrTiO_3$ layer, similar to those previously reported for $SrTiO_3$ buffer layers grown on silicon [17]. These interfacial structural features and their possible origins are further elaborated in the Supporting Information.

### 1.3 | Phase Transitions in $KNbO_3$

To experimentally identify the phase transitions in $KNbO_3$ grown on $SrTiO_3$/Si temperature-dependent second-harmonic generation (SHG) measurements were performed. Electric dipole SHG is a nonlinear optical process, where incident light at frequency $\omega$, is converted into second-harmonic light at twice the frequency, $2\omega$, reflected off the sample. Only materials with a broken inversion symmetry show an SHG response. Figure 3a shows a schematic of the SHG setup used for experiments. Additionally, by rotating the polarization of the incident light, polar plots can be generated by measuring the two orthogonal polarizations ($p$ and $s$ polarized) of the second-harmonic light. Modelling the SHG polar plots reveals the point group symmetry of the material.

Figure 3b shows normal incidence SHG polar plots of $KNbO_3$ grown on $SrTiO_3$/Si at 300 and 600 K. The room temperature SHG polarimetry is fitted to a multidomain orthorhombic (point group $mm2$) model, the expected room temperature phase for single crystal $KNbO_3$. As confirmed from x-ray measurements, the $KNbO_3$ film are strain-relaxed and epitaxial with the $SrTiO_3$ buffer layer; in pseudocubic ($pc$) geometry $KNbO_3$ $[100]_{pc}$ || [100] $SrTiO_3$. In this geometry, the orthorhombic ($or$) unit cell of $KNbO_3$ can be defined with axes parallel to the $[110]_{pc}$, $[1\bar{1}0]_{pc}$, and $[001]_{pc}$ pseudocubic directions [33]. The ferroelectric polarization, parallel to the $[010]_{or}$ (|| $[101]_{pc}$) direction, is 45° with respect to the film surface giving a total of 8 possible domain variants [34, 35] as shown in Figure 3c. As discussed later through PFM measurements, however, a built-in electric field exists in the films which prefers a unique out-of-plane polarization direction, reducing the total domain variants to 4. Since the polarization has both in and out-of-plane components, both oblique and normal incidence SHG response is measurable (Figure S10). The four possible domain variants can be crystallographically represented as: $KNbO_3$ $[100]_{pc}$, $[\bar{1}00]_{pc}$, $[010]_{pc}$ or $[0\bar{1}0]_{pc}$ || [100] $SrTiO_3$ depending on their in-plane polarization directions and can be labelled as $X+$, $X-$, $Y+$ and $Y-$ with area fractions $A_{X+}$, $A_{X-}$, $A_{Y+}$ and $A_{Y-}$, respectively, where $A_{X+} + A_{X-} + A_{Y+} + A_{Y-} = 1$. The out-of-plane polarization component of each of these domains is pointed along the same direction, (either all along $[001]_{pc}$ or $[00\bar{1}]_{pc}$) due to built-in electric field (discussed later). In normal incidence, the SHG polar plots can be described by the following general equation [36] (see Supporting Information):

$$I_i^{2\omega} = K_{1i}\left(\cos^2\theta + K_{2i}\sin^2\theta\right)^2 + K_{3i}\sin^2 2\theta + K_{4i}\left(\cos^2\theta + K_{2i}\sin^2\theta\right) sin2\theta \quad (1)$$

where $i = p$ or $s$ depending on the measured SHG polarization. The nonlinear optical coefficients, $d_{ij}$ (in Voigt notation) of $KNbO_3$ can be related to the extracted fit parameters as follows:

$$\frac{d_0}{d_{32}} = K_{2s} = \frac{1}{K_{2p}} \quad (2)$$

$$\left(\frac{d_{24}}{d_0}\right)^4 = \frac{K_{3s}K_{3p}}{K_{1s}K_{1p}K_{2s}^2}$$

$$\left(\frac{\delta A_X}{\delta A_Y}\right)^4 = \frac{K_{3s}K_{1p}}{K_{1s}K_{3p}K_{2s}^2}$$

$$\cos^2\Gamma = \frac{K_{4p}^2}{4K_{1p}K_{3p}} = \frac{K_{4s}^2}{4K_{1s}K_{3s}}$$

where, $d_0 = d_{15} + (d_{33} + d_{31})/2$, $\delta A_{X(Y)} = A_{X(Y)+} - A_{X(Y)-}$ and $\Gamma = (4\pi l/\lambda)[n_3^{O,2\omega} - n_0^{O,2\omega}]$ is the phase shift in the second-harmonic light generated between domains $X+/X-$ and $Y+/Y-$ due to the birefringence of the film. Here, $n_0^{O,2\omega} = \sqrt{2/[(1/n_1^{O,2\omega})^2 + (1/n_2^{O,2\omega})^2]}$, with $n_1^O$, $n_2^O$, $n_3^O$ representing the principal refractive indices of the orthorhombic unit cell and $l$ is the film thickness. The extracted parameters from $KNbO_3$ on $SrTiO_3$/Si are tabulated in Table 1 in comparison with single crystal $KNbO_3$ reference values [36]. The close match between the measured and expected parameters confirms the orthorhombic phase of unstrained $KNbO_3$ grown on $SrTiO_3$/Si at room temperature. Additionally, $\delta A_X/\delta A_Y = 0.8 \pm 0.1$ reflects an almost equal net poling area fraction of $KNbO_3$ along both the [100] and [010] directions of the $SrTiO_3$ buffer layer. Oblique incidence polar plots can also be similarly fitted with the same general Equation (1), where the K-parameters involve different convolutions of the nonlinear optical coefficients (Figure S10).



15214095, 2026, 63, Downloaded from https://advanced.onlinelibrary.wiley.com/doi/10.1002/adma.75067, Wiley Online Library on [16/11/2026]. See the Terms and Conditions (https://onlinelibrary.wiley.com/terms-and-conditions) on Wiley Online Library for rules of use; OA articles are governed by the applicable Creative Commons License

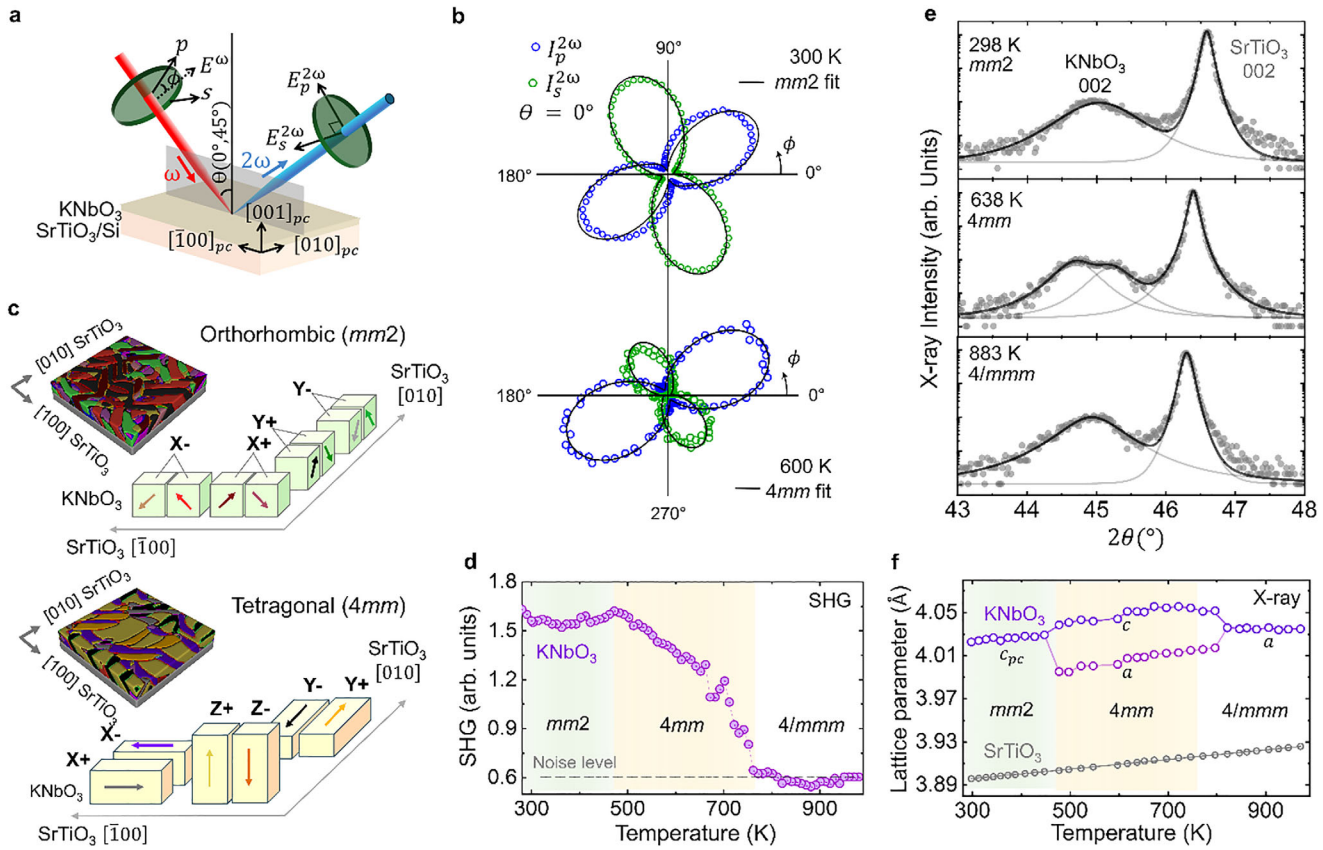



**FIGURE 3** | (a) Schematic of second-harmonic generation (SHG) setup for both normal ($\theta = 0°$) and oblique ($\theta = 45°$) incidence SHG measurements. (b) Normal incidence ($\theta = 0°$) polar plots of $KNbO_3$ on $SrTiO_3$/Si measured at 300 and 600 K. 300 K polar plot is fitted to a multidomain orthorhombic (point group *mm*2) model, while a multidomain tetragonal (point group 4*mm*) model is used to fit polar plots at 600 K. Fitting equations are derived in Supporting Information. (c) Multidomain orthorhombic domain structure used to fit SHG polar plots at 300 K. Inset shows the phase-field microstructure at 450 K, the temperature where the orthorhombic phase fraction is maximized (~80%) in predictions (upper panel). While in general eight orthorhombic domain variants are possible, as discussed later through PFM measurements, the films have a built-in electric field which prefers a unique out-of-plane polarization component. This results in only four domains: $X+$, $X-$, $Y+$, $Y-$, each with only one out-of-plane polarization component. Multidomain tetragonal domain structure used to fit SHG polar plots at 600 K. Inset shows phase-field predicted microstructure at 600 K where the predicted phase fraction of the tetragonal phase is dominant with a phase fraction of ~75%. (lower panel) (d) Temperature-dependent SHG intensity ($I_p^{2\omega}(\phi = 0°)$) measured at normal incidence for $KNbO_3$ on $SrTiO_3$/Si. (e) Lab $\theta - 2\theta$ XRD scans around the 002 $SrTiO_3$ peak. A Pearson VII function is used to fit the XRD peaks [32] (see Supporting Information). At 298 K, the 002 $KNbO_3$ peak is characterized by a single peak, while evolves into a double peak at 638 K (tetragonal phase), eventually becoming a single peak at 883 K (cubic phase). (f) Extracted temperature-dependent lattice parameter of $KNbO_3$ and $SrTiO_3$.

**TABLE 1** | Extracted SHG polar plot fit parameters at 300 K (orthorhombic fit) and 600 K (tetragonal fit). Parameters at 300 K are compared to $KNbO_3$ single crystal reference at 300 K [36]. Parameters at 600 K are compared to reference values on $KNbO_3$ on $SrTiO_3$/MgO films measured at 573 K [35].

| | Orthorhombic | | | Tetragonal | |
|---|---|---|---|---|---|
| **Orthorhombic parameters 300 K** | **$KNbO_3$ on $SrTiO_3$/Si (300 K)** | **Reference (Single crystal, 300 K) [36]** | **Tetragonal Parameters (600 K)** | **$KNbO_3$ on $SrTiO_3$/Si (600 K)** | **Reference (Thin film 573 K) [35]** |
| $\boldsymbol{d_0/d_{32}}$ | $2.8 \pm 0.3$ | 2.56 | $\boldsymbol{d_{33}/d_{31}}$ | $2.1 \pm 0.3$ | $2.5 \pm 0.3$ |
| $\boldsymbol{d_{24}/d_0}$ | $0.5 \pm 0.1$ | 0.45 | $\boldsymbol{d_{15}/d_{33}}$ | $0.4 \pm 0.1$ | $0.4 \pm 0.1$ |
| $\boldsymbol{\delta A_X/\delta A_Y}$ | $0.8 \pm 0.1$ | — | $\boldsymbol{\delta A_X/\delta A_Y}$ | $1.4 \pm 0.1$ | $1.5 \pm 0.2$ |
| **cos Γ** | $\cos\ \Gamma_p = 0.8 \pm 0.1$<br>$\cos\ \Gamma_s = 0.7 \pm 0.1$ | 0.86 | **cos Γ** | $\cos\ \Gamma_p = 0.5 \pm 0.1$<br>$\cos\ \Gamma_s = 0.8 \pm 0.1$ | $0.8 \pm 0.2$ |



15214095, 2026, 63, Downloaded from https://advanced.onlinelibrary.wiley.com/doi/10.1002/adma.75067, Wiley Online Library on [16/11/2026]. See the Terms and Conditions (https://onlinelibrary.wiley.com/terms-and-conditions) on Wiley Online Library for rules of use; OA articles are governed by the applicable Creative Commons License

In contrast, to fit the SHG polarimetry at 600 K a multidomain tetragonal (point group 4*mm*) model was used, the expected phase for single crystal $KNbO_3$. As shown in Figure 3c, six different tetragonal domain variants are considered depending on the orientation of the polarization direction of the $KNbO_3$ unit cell (along [001]) with respect to the $SrTiO_3$ buffer layer. Since $Z+$ and $Z-$ domains are polarized out-of-plane, they do not contribute to a normal incidence SHG signal. From the remaining domains ($X+$, $X-$, $Y+$, $Y-$) with area fractions $A_{X+}$, $A_{X-}$, $A_{Y+}$ and $A_{Y-}$, respectively, expressions to fit the SHG polar plots can be derived to have the same general form as Equation (1), but with different relationship between the *K*-parameters and nonlinear optical coefficients as shown below (see Supporting Information);

$$\frac{d_{33}}{d_{31}} = K_{2s} = \frac{1}{K_{2p}} \tag{3}$$

$$\left(\frac{d_{15}}{d_{33}}\right)^4 = \frac{K_{3s}K_{3p}}{K_{1s}K_{1p}K_{2s}^2}$$

$$\left(\frac{\delta A_X}{\delta A_Y}\right)^4 = \frac{K_{3s}K_{1p}}{K_{1s}K_{3p}K_{2s}^2}$$

$$\cos^2\Gamma = \frac{K_{4p}^2}{4K_{1p}K_{3p}} = \frac{K_{4s}^2}{4K_{1s}K_{3s}}$$

where, $\delta A_{X(Y)} = A_{X(Y)+} - A_{X(Y)-}$ and $\Gamma = (4\pi l/\lambda)[n_3^{T,2\omega} - n_1^{T,2\omega}]$ with $n_1^T$, $n_2^T (= n_1^T)$, $n_3$ representing the principal refractive indices of the tetragonal unit cell. The extracted parameters are tabulated in Table 1 and compared to previous reports on strain relaxed tetragonal $KNbO_3$ thin films at 573 K, showing a close match between them.

It is important to note that while the extracted tensor coefficient ratios agree well with single crystal and thin film references for both the tetragonal and orthorhombic phases, the same general form of Equation (1) can fit both the polar plots. Hence, to conclusively elucidate the phase transition, temperature-dependent x-ray diffraction measurements were performed to measure the out-of-plane lattice parameter of the $KNbO_3$ film. Across the transition, the 002 $KNbO_3$ film peak evolves from a single peak in the orthorhombic phase to a double peak in the tetragonal phase eventually becoming a single peak again in the cubic phase (Figure 3e). All orthorhombic unit cells have the same out-of-plane lattice parameter, while in the tetragonal phase unit cells with out-of-plane ($Z\pm$) and in-plane polarization ($X\pm$, $Y\pm$) have different out-of-plane lattice parameters. Figure 3f shows the temperature evolution of the out-of-plane lattice parameter showing the tetragonal-to-orthorhombic phase transition temperature. This has also been observed previously in strain-relaxed $KNbO_3$ thin films on $SrTiO_3$ substrate [32].

Figure 3d shows the temperature-dependent SHG response of $KNbO_3$ on $SrTiO_3$/Si. The SHG intensity decreases in the tetragonal phase. This is because in the orthorhombic phase, all domain variants generate SHG signal in normal incidence, while in the tetragonal phase only domain variants with in-plane polarization are SHG active [35, 37]. SHG measurements show an orthorhombic-to-tetragonal transition at ~475 K and tetragonal-to-cubic at ~763 K, in agreement with x-ray diffraction measurements. In comparison, single crystal $KNbO_3$ transitions from orthorhombic to tetragonal at ~492 K and from tetragonal to cubic at ~676 K. To further understand the temperature-dependent phase and microstructure evolution, phase-field simulations were performed for strain-relaxed $KNbO_3$ thin films on $SrTiO_3$/Si. Figure S11shows the predicted phase fraction evolution and transition temperatures of the $KNbO_3$ film in agreement with experimental observations. Additionally, rather than exhibiting discrete phase transitions, the simulations reveal mixed phase regions at the transition where one phase gradually grows at the expense of the other. Inset of Figure 3c and Figures S12 and S13 show the temperature evolution of the microstructure of the $KNbO_3$ film, and the averaged polarization averaged across multiple domains.

To confirm the multi-domain nature of the $KNbO_3$ films, room temperature piezo-response force microscopy (PFM) was performed using an interferometric beam displacement sensing PFM (IDS-PFM). Unlike conventional PFM, which utilizes an optical beam deflection system and measures displacement through an angular measurement of the cantilever, IDS-PFM uses an interferometric detection system to measure the absolute physical displacement at the tip-sample contact point [38, 39]. This eliminates global capacitive crosstalk from the cantilever body and enables direct measurement of electromechanical displacement free of electrostatic artifacts (see Supporting Information).

IDS-PFM measurements confirm a spatially varying piezoelectric response with a maximum response reaching ~10 pm $V^{-1}$ across the film (Figure S14). A box-in-box poling experiment, however, reveals no domain switching contrast (Figure S14). We attribute this to the absence of a bottom electrode in the $KNbO_3$ film grown on ~100 nm $SrTiO_3$ buffer layer on silicon. Additional, further switching spectroscopy PFM (SS-PFM) measurements show that whilst points do not indicate reliable switching in both directions, a few are suggestive of switching occurring on one side of the hysteresis loop, resulting in finite switchable polarization and work of switching at those sites (Figure S15).

Additionally, IDS-PFM measurements show a unimodal pixel density distribution centered around 0° phase with no secondary peak at 180° phase difference (Figure S16). A uniform vertical PFM phase across the measured region is consistent with the presence of a built-in electric field (imprint) in the $KNbO_3$ film, which preferentially stabilizes one out-of-plane polarization orientation over the other (either along $[001]_{pc}$ or $[00\bar{1}]_{pc}$). This has previously been observed in $BaTiO_3$ films grown on $SrTiO_3$/Si as well and is attributed to asymmetric charge screening between the top (air) and bottom ($SrTiO_3$/Si) interface or inhomogeneous defect dipoles and surface defects [25, 40]. Phase-field simulations microstructural simulations does not such include a built-in field and hence shows domain variants with either out-of-plane polarization orientation (Figure 3c).

To further elucidate the domain inhomogeneities, SHG microscopy was performed at room temperature. Based on



15214095, 2026, 63, Downloaded from https://advanced.onlinelibrary.wiley.com/doi/10.1002/adma.75067, Wiley Online Library on [16/11/2026]. See the Terms and Conditions (https://onlinelibrary.wiley.com/terms-and-conditions) on Wiley Online Library for rules of use; OA articles are governed by the applicable Creative Commons License

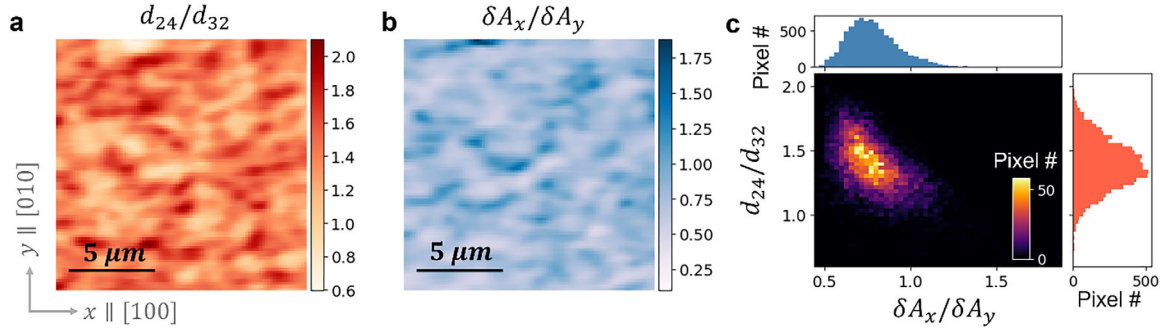



**FIGURE 4** | (a) Map of $d_{24}/d_{32}$ SHG tensor coefficient ratio measured from SHG microscopy (see Supporting Information) across a 15 μm × 15 μm region with a mean $d_{24}/\ d_{32} = 1.4$ in agreement with bulk $KNbO_3$ reference values. The $x$ and $y$-directions shown correspond to the [100] and [010] direction of the $SrTiO_3$ buffer layer. (b) Corresponding map of $\delta A_x/\delta A_y$ across the same region with a mean $\delta A_x/\delta A_y = 0.8$, showing regions preferentially poled along [100] or [010]. (c) Pixel correlated $d_{24}/d_{32}$ versus $\delta A_x/\delta A_y$ depicted as a heat map of the pixel density. Insets show the pixel count histogram of the individual axes showing unimodal distributions.

multidomain orthorhombic model (Equation (1)), by taking SHG microscopy at different combinations of the input and output polarizations, ratios of SHG tensor coefficients and area fraction ratios ($\delta A_X/\delta A_Y$) can be extracted (see Supporting Information). Figure 4a shows the spatial variation of the $d_{24}/d_{32}$ SHG tensor coefficients with a mean value of 1.4 in agreement with single crystal $KNbO_3$ reference values. Maps of other coefficient ratios are shown in Figures S17–19. The spatial variation of the area fraction ratio $\delta A_X/\delta A_Y$ with a mean value of 0.8 is shown in Figure 4b. Region with $\delta A_X/\delta A_Y < 1$, represent a net poling along the [010] direction of the $SrTiO_3$ buffer layer while regions with $\delta A_X/\delta A_Y > 1$ represent a net poling along [100] direction. Figure 4c shows the heat map of the joint distribution of $d_{24}/d_{32}$ versus $\delta A_X/\delta A_Y$.

## 1.4 | Electro-Optic Response of $KNbO_3$ on $SrTiO_3$/Si

The electro-optic effect describes a change in the refractive index, $n$, under an applied electric field $E$, given by $\Delta(\frac{1}{n^2})_{ij} = r_{ijk}\ E_k$, where $r_{ijk}$ is the Pockels tensor describing the linear electro-optic effect and $i$, $j$, $k$ represent dummy subscripts related to the crystal physics axes of the material. Room temperature electro-optic measurements of $KNbO_3$ on $SrTiO_3$/Si were performed at 1550 nm using a polarizer-sample-compensator-analyzer (PSCA) setup [41] as shown in Figure 5a. In this technique, changes in the transmitted intensity of light through a pair of cross polarizers is measured as a function of an applied electric field to the sample. 500 μm square electrodes of 5 nm Ti and 150 nm Pt, with 200 μm spacing were lithographically patterned to apply electric field in the in-plane direction parallel to the [100] direction of the $SrTiO_3$ buffer layer. COMSOL simulations verifying the field distribution between the electrodes are shown in Figure S20.

The incident polarization of light is set to lie along the $[110]_{pc}$ (|| [110] $SrTiO_3$) of the $KNbO_3$ film with the sample rotated 45° away from the incident probe direction. Without an electric field, the unmodulated transmission of light can be described as;

$$I = I_0 \cos^2(\phi + \delta) \tag{4}$$

where, $\phi$ represents the angle through which the analyzer is rotated and $\delta$ is the unmodulated phase accumulated by the beam upon transmitting through the sample and other optical components as shown in Figure 5a. Under an applied electric field, the modulated transmitted intensity, $\Delta I(E)$, can be expressed as;

$$\Delta I\ (E) = I_0\ \Delta\delta\ (E)\ \sin 2\,(\phi + \delta) \tag{5}$$

Figure 5b shows the unmodulated and modulated transmitted intensities at 2 kV $cm^{-1}$ fitted to Equations (4) and (5), respectively. As expected from Equation (4), the modulated intensity maximizes at an analyzer angle corresponding to half transmission of the unmodulated intensity. The induced phase change, $\Delta\delta(E)$, can be converted into electric field induced change in birefringence, $\Delta n = \frac{\Delta\delta\lambda}{2\pi L}$, where $\lambda = 1550$ nm and $L = t/\ cos\ \theta_{film}$ is the path length of light through the sample with $t$ representing the film thickness and $\theta_{film}$ is the angle of beam propagation inside the $KNbO_3$ film (see Supporting Information). An effective electro-optic coefficient is derived according to $r_{eff} = \frac{2\Delta n}{n^3 E} = 113\ \pm 12$ pm $V^{-1}$, for a 18 nm thick film, where $n = 2.20$ is the refractive index of $KNbO_3$ at 1550 nm [5].

To investigate the effect of thickness, electro-optic measurements on thicker $KNbO_3$ thin films (48 and 96 nm) were performed. As shown in Figure 5c, a linear response is observed in all measured thicknesses signifying Pockels effect as the origin of the electro-optic response and yields an $r_{eff} = 91 \pm 5$ pm $V^{-1}$ for the 48 nm film and $146 \pm 14$ pm $V^{-1}$ for the 96 nm film in comparison to $113 \pm 12$ pm $V^{-1}$ for the 18 nm film. All three thicknesses possess similar electro-optic response, which is expected given the strain-relaxed nature of all the three films measured. Electro-optic measurements performed on $SrTiO_3$/Si show no electric field induced change in $\Delta n$ confirming the electro-optic response to originate in the $KNbO_3$ film alone.

Additionally, the experimentally measured electro-optic response closely matches the phase-field predicted microstructure-averaged electro-optic response of $KNbO_3$ grown on $SrTiO_3$/Si at 300 K converted to a $r_{eff} = 88$ pm $V^{-1}$ (Figure 5d), based on experimental geometry (see Supporting Information). The predicted temperature evolution of the electro-optic coefficients



15214095, 2026, 63, Downloaded from https://advanced.onlinelibrary.wiley.com/doi/10.1002/adma.75067, Wiley Online Library on [16/11/2026]. See the Terms and Conditions (https://onlinelibrary.wiley.com/terms-and-conditions) on Wiley Online Library for rules of use; OA articles are governed by the applicable Creative Commons License

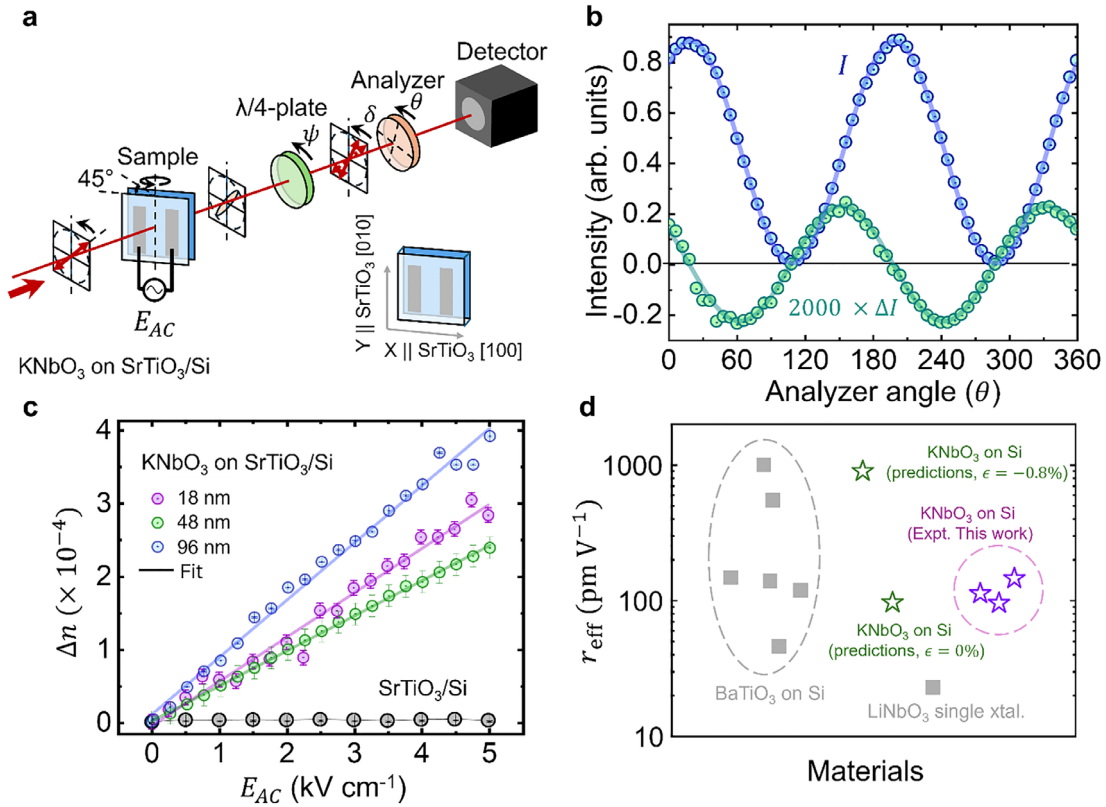



**FIGURE 5** | (a) Schematic of the electro-optics setup used for measurements. Inset shows the crystallographic direction of the $SrTiO_3$ buffer layer in laboratory frame ($X$, $Y$, $Z$). (b) Unmodulated and modulated transmission intensities through the $KNbO_3$ on $SrTiO_3$/Si sample. The modulated intensity was measured under a 2 kV cm$^{-1}$ and 555 Hz AC electric field. (c) Change in refractive index ($\Delta n$) versus applied AC electric field amplitude ($E_{AC}$) measured in three different $KNbO_3$ film thicknesses grown on $SrTiO_3$/Si and compared to the $SrTiO_3$/Si substrate. (d) Comparison of room temperature $r_{eff}$ for $KNbO_3$ on $SrTiO_3$/Si and other related materials measured using the same technique in transmission geometry (Table S2). The phase-field predicted microstructure averaged electro-optic tensor is converted to $r_{eff}$ based on experimental measurement geometry (see Supporting Information). A modest compressive strain of − 0.8% is predicted to enhance $r_{eff}$ to ~900 pm V$^{-1}$. This is compared to thin films of $BaTiO_3$ on Si [2, 42–46], and $LiNbO_3$ [41] single crystals.

is shown in Figure S13. Phase-field simulated wavelength dispersion of the electro-optic response is shown in Figure S21. While the strain-relaxed films established here yield $r_{eff}$ = 146 ± 14 pm V$^{-1}$, phase-field simulations reveal substantial room for improvement through epitaxial strain engineering. Under compressive strain, a monoclinic phase is stabilized at low temperatures while a tetragonal phase persists at high temperatures, with the tetragonal-to-monoclinic phase transition temperature tunable by an epitaxial strain. At the phase boundary, large enhancements in the electro-optic response are predicted, reaching up to $r_{eff}$ ~900 pm V$^{-1}$ at 300 K for a − 0.8% compressive strain. This enhancement can also be achieved through compositional tuning in the (K,Na)$NbO_3$ system, where sodium substitution introduces a chemical strain that drives analogous phase boundary engineering and electro-optic enhancement [7].

This behavior can be understood within the thermodynamic theory of the electro-optic effect. For example, the $r_{51}$ ($r_{131}$ in uncontracted notation) electro-optic coefficient can be expressed as [41, 47]:

$$r_{131} = \left(\frac{\partial B_{13}}{\partial E_1}\right) \cong \left(\frac{\partial B_{13}}{\partial P_1^L}\right)\left(\frac{\partial P_1^L}{\partial E_1}\right) = f_{131}^L \chi_{11}^L \qquad (6)$$

where $B_{ij} = \left(\frac{1}{n^2}\right)_{ij}$ is the optical dielectric stiffness, $P_i^L$ is the lattice polarization, $f_{131}^L$ is the linear polar-optic coefficient, and $\chi_{11}^L$ is the lattice dielectric susceptibility. Since $f_{131}^L$ is proportional to the spontaneous polarization and remains roughly constant under compressive strain, the enhancement is primarily driven by the increase of $\chi_{11}^L$ near the phase boundary. By adjusting the compressive strain or composition, the temperature window of this enhancement can be positioned at any desired operating temperature [5, 41].

## 2 | Conclusion

Our results show that high-quality, crystalline $KNbO_3$ films can be grown on silicon substrates using $SrTiO_3$ buffer layers via sub-oxide molecular-beam epitaxy. X-ray diffraction and transmission electron microscopy confirm epitaxy with excellent crystalline quality, while the films exhibit strain-relaxed characteristics. Second-harmonic generation measurements and x-ray diffraction supported by phase-field simulations, reveal phase transitions and nonlinear optical coefficients comparable to single crystal $KNbO_3$, consistent with the relaxed strain state of the films. Significantly, electro-optic measurements demonstrate a response



15214095, 2026, 63, Downloaded from https://advanced.onlinelibrary.wiley.com/doi/10.1002/adma.75067, Wiley Online Library on [16/11/2026]. See the Terms and Conditions (https://onlinelibrary.wiley.com/terms-and-conditions) on Wiley Online Library for rules of use; OA articles are governed by the applicable Creative Commons License

of 146 ± 14 pm $V^{-1}$, confirming that $KNbO_3$ retains substantial electro-optic activity when integrated on silicon.

As shown in Figure 5d, phase-field predictions further suggest that under modest compressive strain, the electro-optic response can be enhanced to ~900 pm $V^{-1}$[8]. This strain tunability can be achieved on silicon platforms by employing compositionally graded (Ba,Sr)$TiO_3$ [23, 24] buffer layers instead of pure $SrTiO_3$. By varying the barium concentration, the lattice parameter of the buffer layer can be systematically tuned, imposing controlled epitaxial strain on the $KNbO_3$ film. Alternatively, compositionally graded $SrSn_xTi_{1-x}O_3$ or $SrGe_xTi_{1-x}O_3$ buffer layers can also be used to achieve tunable lattice parameters required to strain the $KNbO_3$ film [25, 26].

$KNbO_3$'s intrinsically strong piezoelectric response and electrostrictive effect [8], combined with the epitaxial silicon integration demonstrated here, provides a pathway towards on-chip acoustic wave devices and piezo-optomechanical systems [15]. The nonlinear optical properties demonstrated through second-harmonic generation suggest potential applications in frequency conversion and all-optical signal processing integrated directly with silicon photonic circuits [48], particularly transceivers of interest currently for optical interconnects employed in data centers. Furthermore, the ferroelectric nature of this material system opens possibilities for non-volatile memory elements integrated with photonic and electronic components, enabling novel computing architectures that merge logic, memory, and optical interconnects on a single chip.

## 3 | Methods

### 3.1 | Thin Film Synthesis and Characterization

#### 3.1.1 | $KNbO_3$ on $SrTiO_3$ Substrates

$KNbO_3$ on $SrTiO_3$ films were grown using a Vecco Gen 10 MBE system, with a 10.6 μm $CO_2$ laser substrate heater from Epiray GmbH (THERMALAS Substrate heater). A description of the preparation of the $Nb_2O_5$, potassium effusion cells, flux calibration with quartz crystal microbalance (QCM), RHEED pattern monitoring and growth of $KNbO_3$ thin films on $GdScO_3$ and $DyScO_3$ substrates is elaborated elsewhere [8].

#### 3.1.2 | Epitaxial Thin Films of $SrTiO_3$ on Si

100 nm of $SrTiO_3$ was deposited on a 3-inch (300 μm thick) Si wafer which was prepared according to the detailed description reported previously [17]. The Si wafer was deoxidized with a buffered HF solution before deposition. 2.5 Unit cells of $SrTiO_3$ were deposited at 300°C followed by an anneal at 500°C. This process was repeated 3 times before the remaining 249 unit cells were deposited at 550°C at a background pressure of $8.5 \times 10^{-9}$ torr resulting in a total film thickness of 100 nm. After deposition, the wafer was diced into 10 × 10 $mm^2$ pieces, cleaned with acetone, IPA and deionized water before loading individual 10 × 10 $mm^2$ pieces back into the MBE system for subsequent deposition of $KNbO_3$.

### 3.2 | Thermodynamic Simulation

Thermodynamic calculations were carried out using the Thermo-Calc software [49] and the SGTE Substance Database (SSUB5) [50]. Missing thermodynamic data for $KNbO_3$, $KNb_3O_8$, $K_4Nb_6O_{17}$, and $KNb_8O_{14}$ were incorporated into SSUB5 using density-functional-theory (DFT) based data from the Materials Project [51]. These values were implemented through the following formation reactions:

$$K_2O + Nb_2O_5 = 2\ KNbO_3 \quad \text{(R1)}$$

$$K_2O + 3\ Nb_2O_5 = 2\ KNb_3O_8 \quad \text{(R2)}$$

$$2K_2O + 3\ Nb_2O_5 = K_4Nb_6O_{17} \quad \text{(R3)}$$

$$K_2O + 6\ NbO + 8\ NbO_2 + Nb_2O_5 = 2\ KNb_8O_{14} \quad \text{(R4)}$$

The reaction Gibbs energies obtained from the Materials Project [50] for Reactions (R1)–(R4) are −34.5, −17.2, −27.9, and −10.7 kJ/mol-atom, respectively.

Figure 1a shows the calculated pressure-temperature phase diagram for the K-Nb-O system at a fixed $O_2$ partial pressure of 7.5 $\times 10^{-4}$ Torr (corresponding to an oxygen activity of $10^{-6}$). Under these conditions, the stability window for $KNbO_3$ lies near the center of the diagram. As an example, Figure S1 shows the calculated K-Nb-O2 isothermal phase diagram at 1000 K under a total pressure of 1 atm calculated using the present thermodynamic database.

### 3.3 | Synchrotron Based X-Ray Reciprocal Space Mapping

Synchrotron x-ray diffraction measurements were performed at the ID4B (QM2) beamline of Cornell high energy synchrotron source (CHESS) at an incident x-ray energy was 20 keV with an area detector array (Pilatus 6 M). This is further elaborated elsewhere [8, 41].

### 3.4 | Transmission Electron Microscopy

The sample lamellae were fabricated using a Thermo Fisher Scientific Scios 2 dual-beam FIB–SEM. To protect the surface during milling, two Pt capping layers were deposited: electron-beam deposition (3.2 nA) followed by Ga ion-beam deposition (0.26 nA). Two lamellae, each ~1 μm thick, were lifted out from the region of interest with the in-plane x-direction aligned to the $SrTiO_3$ [100] and [110] directions, respectively, and mounted on a half-grid. To reduce ion-beam damage, the lamella was thinned under Ga ions while progressively lowering the accelerating voltage from 30 to 2 kV (30, 16, 8, 5, and 2 kV). Both specimens reached an estimated thickness of ~70 nm in the target area.



15214095, 2026, 63, Downloaded from https://advanced.onlinelibrary.wiley.com/doi/10.1002/adma.75067, Wiley Online Library on [16/11/2026]. See the Terms and Conditions (https://onlinelibrary.wiley.com/terms-and-conditions) on Wiley Online Library for rules of use; OA articles are governed by the applicable Creative Commons License

Cross-sectional STEM measurements were carried out using an aberration-corrected 300 kV FEI Titan G2 60/300 S/TEM. The microscope was operated with a 70 µm C2 condenser aperture, spot size 8, 115 mm camera length, and a probe convergence semi-angle of 25.2 mrad. HAADF signals were recorded over 42–244 mrad, and images were obtained with a probe current of 0.07 nA. EDS data were acquired using a Super-X detector array, and the spectra were processed in Bruker Esprit software. Post-processing of the EDS maps included 1/4 Q-map binning, spectral deconvolution via series-fit, and quantitative analysis using P/B ZAF method. For visualization, brightness and gamma setting were applied to every elemental channel to maintain consistent rendering.

### 3.5 | Second-Harmonic Generation Measurements

Temperature-dependent second-harmonic generation (SHG) polarimetry were measured using at a fundamental wavelength of 800 nm generated by a Spectra-Physics Solstice Ace Ti:Sapphire laser with an 80 MHz repetition rate and 300 fs pulse width. Room temperature SHG microscopy was performed in normal incidence reflection geometry with the fundamental laser beam focused by a high-NA objective (0.75 NA). This is further elaborated elsewhere [8, 41].

### 3.6 | Phase-Field Simulations

Phase-field simulations of the structural and optical properties are discussed in detail elsewhere [5, 41]. A table containing all coefficients used in the phase-field simulations relevant for $KNbO_3$ is given in the supplementary material (Table S1). For the simulations, a system size of 128 $\Delta x_1 \times 128\ \Delta x_2 \times 36\ \Delta x_3$ is used. There are 12 $\Delta x_3$ grid points for the substrate where the elastic constants are assumed to be the same as the ferroelectric film, and there are 9 $\Delta x_3$ grid points acting as an air layer above the film. The thickness of $KNbO_3$ is set to be 15 $\Delta x_3$. Periodic boundary conditions are used along the in-plane lateral directions, and natural boundary conditions are used along the film-substrate and film-air interfaces. The interface between the film and the substrate is assumed to be relaxed, and hence the in-plane misfit strain is set to:

$$\varepsilon_{11} = 0, \varepsilon_{22} = 0, \varepsilon_{12} = \varepsilon_{21} = 0$$

The simulations begin with an initial condition of $P_i^L$ ($x_i$, t = 0) = [0.0 0.0 0.1 C $m^{-2}$] + $\Delta P^{noise}$ ($x_i$,t = 0), where, $P^i_L$ ($x_i$,t) is the lattice polarization and $|P^{noise}|$ = 0.1 C $m^{-2}$, and relax for 20,000 time steps. O simulate the evolution of the polarization under an applied electric field and the corresponding electro-optic effect, a uniform electric field is applied along the $[100]_{pc}$ direction ranging from −70 kV $cm^{-1}$ to 70 kV $cm^{-1}$ which varies in time with a sinewave, with one period of the being equal to 65,000 time steps. The linear electro-optic effect is found by taking the average of the refractive index over the ferroelectric material as a function of an applied electric field and fitting to a cubic polynomial centred at zero. The phase fractions were determined by sorting the local lattice polarization vectors according to the minimum angular deviation from the ideal crystallographic polarization directions assuming the presence of only tetragonal, orthorhombic and rhombohedral domains. The lattice–polarization evolution was computed using the Mu-Pro phase-field simulation package.

### 3.7 | Electro-Optic Measurement

Electro-optic measurements were performed using a homebuilt polarizer-sample-compensator-analyzer (PSCA) setup with a 1550 nm HP 81689A continuous-wave laser source. A Nirvana 2017 balanced detector was used for measurements with Stanford SR830 lock-in amplifier. An AC modulation was applied to the sample at 555 Hz frequency with an Agilent 33220A signal generator amplified by a TREK 610C high voltage amplifier. This is further elaborated elsewhere [41].

#### Author Contributions

**Sankalpa Hazra**: conceptualization, investigation, writing – original draft, writing – review and editing, visualization, methodology, validation, data curation, formal analysis. **Tobias Schwaigert**: conceptualization, investigation, visualization, writing – original draft, writing – review and editing, validation, methodology. **Yingxin Zhu**: investigation, visualization, formal analysis. **Aiden Ross**: investigation, visualization, formal analysis, writing – review and editing, software. **Muhammad Aminul Haque Chowdhury**: investigation. **Shun-Li Shang**: investigation, writing – review and editing, formal analysis. **Sameer Singh**: investigation. **Zhiyu Zhang**: investigation. **Zhe Wang**: investigation. **Brynn Brower**: investigation. **Saugata Sarker**: investigation. **Suchismita Sarker**: investigation, funding acquisition, resources, writing – review and editing. **Zi-Kui Liu**: resources, supervision, writing – review and editing, funding acquisition. **Long-Qing Chen**: resources, supervision, funding acquisition, formal analysis, writing – review and editing. **Yang Yang**: investigation, writing – review and editing, supervision, funding acquisition. **Darrell G. Schlom**: conceptualization, writing – original draft, validation, writing – review and editing, supervision, project administration. **Venkatraman Gopalan**: conceptualization, investigation, funding acquisition, writing – review and editing, project administration, supervision, resources.

#### Acknowledgements

S.H., V.G. acknowledge support from the National Science Foundation grant DMREF-2522897 for thin film synthesis, electro-optic measurements, SHG measurements, x-ray experiments, and manuscript preparation. A.R., L.Q.C., and V.G. acknowledge support from the National Science Foundation grant DMREF-2522897 for the phase-field simulations. A.R. also acknowledges the support of the National Science Foundation Graduate Research Fellowship Program under Grant Number. DGE1255832. The phase-field simulations in this work were conducted with the advanced computing resources provided by Texas A&M High Performance Research Computing, through allocation MAT250123 from the ACCESS program, which is supported by National Science Foundation Grants Nos. 2138259, 2138286, 2138307, 2137603, and 2138296. M.A.H.C. acknowledges support from the National Science Foundation grant DMREF-2522897 for sample preparation, partial S.H.G. and x-ray characterization. B.B. acknowledges support from the National Science Foundation grant DMREF-2522897 for partial electro-optic measurements. The $KNbO_3$ thin films were synthesized at the Platform for the Accelerated Realization, Analysis, and Discovery of Interface Materials (PARADIM), which is supported by the National Science Foundation (NSF) under Cooperative Agreement No. DMR-2039380. T.S. and D.G.S. acknowledge support from the NSF through PARADIM



15214095, 2026, 63, Downloaded from https://advanced.onlinelibrary.wiley.com/doi/10.1002/adma.75067, Wiley Online Library on [16/11/2026]. See the Terms and Conditions (https://onlinelibrary.wiley.com/terms-and-conditions) on Wiley Online Library for rules of use; OA articles are governed by the applicable Creative Commons License

under Cooperative Agreement No. DMR-2039380. This work is based on research conducted at the Center for High-Energy X-ray Sciences (CHEXS), which is supported by the National Science Foundation (BIO, ENG and MPS Directorates) under award DMR-2342336. Sameer Singh acknowledges support from National Science Foundation through grant NSF-SITE PHYS-25349159 and MRSEC: DMR-2011839 for partial SHG and x-ray characterization. Y.Z., Z.Z., and Y.Y. acknowledge the Institute for Computational and Data Sciences (ICDS) Quantum SuperSEED grant. The interferometric PFM was conducted at the Center for Nanophase Materials Science, which is a US Department of Energy, Office of Science User Facility at Oak Ridge National Laboratory. This research used resources of the Center for Functional Nanomaterials (CFN) which is US Department of Energy Office of Science user facilities at Brookhaven National Laboratory, under contract DE-SC0012704.

## Conflicts of Interest

The authors have a provisional patent filed on this work. Long-Qing Chen has a financial interest in MuPRO, LLC, a company which licenses and markets the software package used in this research.

## Data Availability Statement

The data that supports the findings of this study are available within the article. Datasets used for the generation of figures presented in the article is available at https://doi.org/10.6084/m9.figshare.33920134. Additional data related to the film growth and structural characterization is available at https://doi.org/10.34863/ssec-tz95.

## References

1. M. P. Warusawithana, C. Cen, C. R. Sleasman, et al., "A Ferroelectric Oxide Made Directly on Silicon," *Science (1979)* 324 (2009): 367.

2. S. Abel, T. Stöferle, C. Marchiori, et al., "A Strong Electro-Optically Active Lead-Free Ferroelectric Integrated on Silicon," *Nature Communications* 4 (2013): 1671, https://doi.org/10.1038/ncomms2695.

3. G. Sinatkas, T. Christopoulos, O. Tsilipakos, and E. E. Kriezis, "Electro-Optic Modulation in Integrated Photonics," *Journal of Applied Physics* 130 (2021): 010901, https://doi.org/10.1063/5.0048712.

4. X. Chen, J. Lin, and K. Wang, "A Review of Silicon-Based Integrated Optical Switches," *Laser & Photonics Reviews* 17 (2023): 2200571, https://doi.org/10.1002/lpor.202200571.

5. A. Ross, V. Gopalan, and L.-Q. Chen, "Thermodynamics of Ferroelectric and Optical Properties in KNbO3," preprint, ArXiv, January 23, 2026, https://doi.org/10.48550/arXiv.2601.17150.

6. P. Günter, "Electro-Optical Properties of $KNbO_3$," *Optics Communication* 11 (1974): 285, https://doi.org/10.1016/0030-4018(74)90183-7.

7. B. Wang, H.-N. Chen, J.-J. Wang, and L.-Q. Chen, "Ferroelectric Domain Structures and Temperature-Misfit Strain Phase Diagrams of $K_{1-x}Na_xNbO_3$ Thin Films: A Phase-Field Study," *Applied Physics Letters* 115 (2019): 092902, https://doi.org/10.1063/1.5116910.

8. S. Hazra, T. Schwaigert, A. Ross, et al., "Colossal Strain Tuning of Ferroelectric Transitions in $KNbO_3$ Thin Films," *Advanced Materials* 36 (2024): 2408664, https://doi.org/10.1002/adma.202408664.

9. Y. L. Li, L. E. Cross, and L. Q. Chen, "A Phenomenological Thermodynamic Potential for $BaTiO_3$ Single Crystals," *Journal of Applied Physics* 98 (2005): 064101, https://doi.org/10.1063/1.2042528.

10. M. J. Haun, E. Furman, S. J. Jang, H. A. McKinstry, and L. E. Cross, "Thermodynamic Theory of $PbTiO_3$," *Journal of Applied Physics* 62 (1987): 3331, https://doi.org/10.1063/1.339293.

11. C. Ederer and N. A. Spaldin, "Effect of Epitaxial Strain on the Spontaneous Polarization of Thin Film Ferroelectrics," *Physical Review Letters* 95 (2005): 257601, https://doi.org/10.1103/PhysRevLett.95.257601.

12. W. Jiang, C. J. Sarabalis, Y. D. Dahmani, et al., "Efficient Bidirectional Piezo-Optomechanical Transduction Between Microwave and Optical Frequency," *Nature Communications* 11 (2020): 1166.

13. T. T. A. Lummen, J. Leung, A. Kumar, et al., "Emergent Low-Symmetry Phases and Large Property Enhancements in Ferroelectric $KNbO_3$ Bulk Crystals," *Advanced Materials* 29 (2017): 1700530, https://doi.org/10.1002/adma.201700530.

14. M. Schmidbauer, D. Braun, T. Markurt, M. Hanke, and J. Schwarzkopf, "Strain Engineering of Monoclinic Domains in $K_xNa_{1-x}NbO_3$ Epitaxial Layers: A Pathway to Enhanced Piezoelectric Properties," *Nanotechnology* 28 (2017): 24LT02, https://doi.org/10.1088/1361-6528/aa715a.

15. L. von Helden, M. Schmidbauer, S. Liang, M. Hanke, R. Wördenweber, and J. Schwarzkopf, "Ferroelectric Monoclinic Phases in Strained $K_{0.70}Na_{0.30}NbO_3$ Thin Films Promoting Selective Surface Acoustic Wave Propagation," *Nanotechnology* 29 (2018): 415704.

16. Y.-C. Chang, C. Wang, S. Yin, R. C. Hoffman, and A. G. Mott, "Giant Electro-Optic Effect in Nanodisordered KTN Crystals," *Optics Letters* 38 (2013): 4574, https://doi.org/10.1364/OL.38.004574.

17. Z. Wang, B. H. Goodge, D. J. Baek, et al., "Epitaxial $SrTiO_3$ Film on Silicon With Narrow Rocking Curve Despite Huge Defect Density," *Physical Review Materials* 3 (2019): 073403, https://doi.org/10.1103/PhysRevMaterials.3.073403.

18. J. Kim, M. Yu, J.-W. Lee, et al., "Electronic-Grade Epitaxial (111) $KTaO_3$ Heterostructures," *Science Advances* 10 (2024): eadk4288, https://doi.org/10.1126/sciadv.adk4288.

19. T. Schwaigert, S. Salmani-Rezaie, M. R. Barone, et al., "Molecular Beam Epitaxy of $KTaO_3$," *Journal of Vacuum Science & Technology A* 41 (2023): 022703, https://doi.org/10.1116/6.0002223.

20. D. G. Schlom and J. S. Harris, "*MBE Growth of High Tc Superconductors*," in *Molecular Beam Epitaxy: Applications to Key Materials*, ed. R. F. C. Farrow, (1995).

21. G. Shirane, R. Newnham, and R. Pepinsky, "Dielectric Properties and Phase Transitions of $NaNbO_3$ and $(Na,K)NbO_3$," *Physical Review*, 96, no. 3 (1954), 581–588, https://doi.org/10.1103/physrev.96.581.

22. H. M. H. Mori and H. I. H. Ishiwara, "Epitaxial Growth of $SrTiO_3$ Films on Si(100) Substrates Using a Focused Electron Beam Evaporation Method," *Japanese Journal of Applied Physics* 30 (1991): L1415, https://doi.org/10.1143/JJAP.30.L1415.

23. R. Gupta, V. Gupta, and M. Tomar, "Structural and Dielectric Properties of PLD Grown BST Thin Films," *Vacuum* 159 (2019): 69, https://doi.org/10.1016/j.vacuum.2018.10.010.

24. V. Vaithyanathan, J. Lettieri, W. Tian, et al., "C -axis Oriented Epitaxial $BaTiO_3$ Films on (001) Si," *Journal of Applied Physics* 100 (2006): 024108, https://doi.org/10.1063/1.2203208.

25. J. Zhao, M. Ahmadi, B. Noheda, and M. F. Sarott, "Integration of Imprint-Free and Low Coercivity Ferroelectric $BaTiO_3$ Thin Films on Silicon," *Nano Letters* 26 (2026): 764, https://doi.org/10.1021/acs.nanolett.5c05139.

26. S. Ismail-Beigi, F. J. Walker, S.-W. Cheong, K. M. Rabe, and C. H. Ahn, "Alkaline Earth Stannates: The Next Silicon?," *APL Materials* 3 (2015): 062510, https://doi.org/10.1063/1.4921338.

27. J. Ramdani, R. Droopad, Z. Yu, et al., "Interface Characterization of High-quality $SrTiO_3$ Thin Films on Si(100) Substrates Grown by Molecular Beam Epitaxy," *Applied Surface Science* 159–160 (2000): 127, https://doi.org/10.1016/S0169-4332(00)00050-7.

28. H. Li, J. Finder, Y. Liang, R. Gregory, and W. Qin, "Dielectric Properties of Epitaxial $Ba_{0.5}Sr_{0.5}TiO_3$ Films on Amorphous $SiO_2$ on Sapphire," *Applied Physics Letters* 87 (2005): 072905, https://doi.org/10.1063/1.2011774.

29. L. V. Goncharova, D. G. Starodub, and E. Garfunkel, "Interface Structure and Thermal Stability of Epitaxial $SrTiO_3$ Thin Films on Si(001)," *Journal of Applied Physics* 100, (2006): 014912, https://doi.org/10.1063/1.2206710.



15214095, 2026, 63, Downloaded from https://advanced.onlinelibrary.wiley.com/doi/10.1002/adma.75067, Wiley Online Library on [16/11/2026]. See the Terms and Conditions (https://onlinelibrary.wiley.com/terms-and-conditions) on Wiley Online Library for rules of use; OA articles are governed by the applicable Creative Commons License

30. P. Ahmet, T. Koida, M. Takakura, et al., "Diffusion Induced Amorphization in the Crystalline $SrTiO_3$ Thin Films Grown on Si (1 0 0) Investigated by Combinatorial Method," *Applied Surface Science* 189 (2002): 307, https://doi.org/10.1016/S0169-4332(01)01008-X.

31. Z. Yu, Y. Liang, C. Overgaard, et al., "Advances in Heteroepitaxy of Oxides on Silicon," *Thin Solid Films* 462–463 (2004): 51, https://doi.org/10.1016/j.tsf.2004.05.088.

32. V. Gopalan and R. Raj, "In-Situ X-Ray Diffraction Study of Phase Transitions in Epitaxial $KNbO_3$ Thin Films," *Ferroelectrics* 200 (1997): 343, https://doi.org/10.1080/00150199708008617.

33. V. Gopalan and R. Raj, "Domain Structure-Second Harmonic Generation Correlation in Potassium Niobate Thin Films Deposited on a Strontium Titanate Substrate," *Journal of the American Ceramic Society* 79 (1996): 3289, https://doi.org/10.1111/j.1151-2916.1996.tb08107.x.

34. S. A. Denev, T. T. A. Lummen, E. Barnes, A. Kumar, and V. Gopalan, "Probing Ferroelectrics Using Optical Second Harmonic Generation," *Journal of the American Ceramic Society* 94 (2011): 2699, https://doi.org/10.1111/j.1551-2916.2011.04740.x.

35. V. Gopalan and R. Raj, "Domain Structure and Phase Transitions in Epitaxial $KNbO_3$ Thin Films Studied by In Situ Second Harmonic Generation Measurements," *Applied Physics Letters* 68 (1996): 1323, https://doi.org/10.1063/1.115922.

36. V. Gopalan and R. Raj, "Electric Field Induced Domain Rearrangement in Potassium Niobate Thin Films Studied by In Situ Second Harmonic Generation Measurements," *Journal of Applied Physics* 81 (1997): 865, https://doi.org/10.1063/1.364222.

37. V. Gopalan and R. Raj, "Structure-Optical Property Correlation of Epitaxial Potassium Niobate Thin Films Deposited on Magnesium Oxide (100) Substrates Using a Strontium Titanate Transition Layer," *Journal of the American Ceramic Society* 78 (1995): 1825, https://doi.org/10.1111/j.1151-2916.1995.tb08895.x.

38. L. Collins, Y. Liu, O. S. Ovchinnikova, and R. Proksch, "Quantitative Electromechanical Atomic Force Microscopy," *ACS Nano* 13 (2019): 8055, https://doi.org/10.1021/acsnano.9b02883.

39. K. P. Kelley, L. Li, Y. Ren, et al., "Tensor Factorization for Elucidating Mechanisms of Piezoresponse Relaxation via Dynamic Piezoresponse Force Spectroscopy," *NPJ Computational Materials* 6 (2020): 113, https://doi.org/10.1038/s41524-020-00384-6.

40. I. Olaniyan, A. B. Martínez, V. V. Hevelke, et al., "Optically Induced Irreversible Ferroelastic and Ferroelectric Switching in Epitaxial $BaTiO_3$ Films," *ACS Nano* 19 (2025): 37534.

41. A. Suceava, S. Hazra, A. Ross, et al., "Colossal Cryogenic Electro-Optic Response Through Metastability in Strained $BaTiO_3$ Thin Films," *Advanced Materials* 38 (2026): 07564, https://doi.org/10.1002/adma.202507564.

42. K. Alexander, A. Benyamini, D. Black, et al., "A Manufacturable Platform for Photonic Quantum Computing," *Nature* 641 (2025): 876.

43. M. Reynaud, M. Waqar, C. Du, A. B. Posadas, X. Pan, and A. A. Demkov, "Enhancement of Electro-optic Response in $BaTiO_3$ Films Integrated on Si via Heating and Cooling Rate Control," *Communications Materials* 6 (2025): 176, https://doi.org/10.1038/s43246-025-00908-x.

44. K. J. Kormondy, Y. Popoff, M. Sousa, et al., "Microstructure and Ferroelectricity of $BaTiO_3$ Thin Films on Si for Integrated Photonics," *Nanotechnology* 28 (2017): 075706, https://doi.org/10.1088/1361-6528/aa53c2.

45. K. J. Kormondy, S. Abel, F. Fallegger, et al., "Analysis of the Pockels Effect in Ferroelectric Barium Titanate Thin Films on Si(001)," *Microelectronic Engineering* 147 (2015): 215, https://doi.org/10.1016/j.mee.2015.04.041.

46. M. Reynaud, H. Huyan, C. Du, et al., "Si-Integrated $BaTiO_3$ for Electro-Optic Applications: Crystalline and Polarization Orientation Control," *ACS Appl Electron Mater* 5 (2023): 4605, https://doi.org/10.1021/acsaelm.3c00747.

47. A. Ross, M. S. M. M. Ali, A. Saha, et al., "Thermodynamic Theory of Linear Optical and Electro-Optical Properties of Ferroelectrics," *Physical Review B* 111 (2025): 085109, https://doi.org/10.1103/PhysRevB.111.085109.

48. M. Borghi, C. Castellan, S. Signorini, A. Trenti, and L. Pavesi, "Nonlinear Silicon Photonics," *Journal of Optics* 19 (2017): 093002, https://doi.org/10.1088/2040-8986/aa7a6d.

49. J.-O. Andersson, T. Helander, L. Höglund, P. Shi, and B. Sundman, "Thermo-Calc & DICTRA, Computational Tools for Materials Science," *Calphad* 26 (2002): 273, https://doi.org/10.1016/S0364-5916(02)00037-8.

50. A. Jain, S. P. Ong, G. Hautier, et al., "Commentary: The Materials Project: A Materials Genome Approach to Accelerating Materials Innovation," *APL Materials* 1 (2013): 011002, https://doi.org/10.1063/1.4812323.

51. Scientific Group Thermodata Europe (SGTE), Lehrstuhl fuer Theoretische Huettenkunde (Ed.), *Landolt-Boernstein New Ser. Gr.* IV, (Springer 1999).

## Supporting Information

Additional supporting information can be found online in the Supporting Information section.

**Supporting File**: adma75067-sup-0001-SuppMat.docx.



15214095, 2026, 63, Downloaded from https://advanced.onlinelibrary.wiley.com/doi/10.1002/adma.75067, Wiley Online Library on [16/11/2026]. See the Terms and Conditions (https://onlinelibrary.wiley.com/terms-and-conditions) on Wiley Online Library for rules of use; OA articles are governed by the applicable Creative Commons License

**Supporting Information**

# Epitaxially integrated Electro-Optic $KNbO_3$ thin films on Silicon

*Sankalpa Hazra*, Tobias Schwaigert*, Yingxin Zhu, Aiden Ross, Muhammad Aminul Haque Chowdhury, Shun-Li Shang, Sameer Singh, Zhiyu Zhang, Zhe Wang, Brynn Brower, Saugata Sarker, Suchismita Sarker, Zi-Kui Liu, Rama K Vasudevan, Long-Qing Chen, Yang Yang, Darrell G. Schlom and Venkatraman Gopalan.*

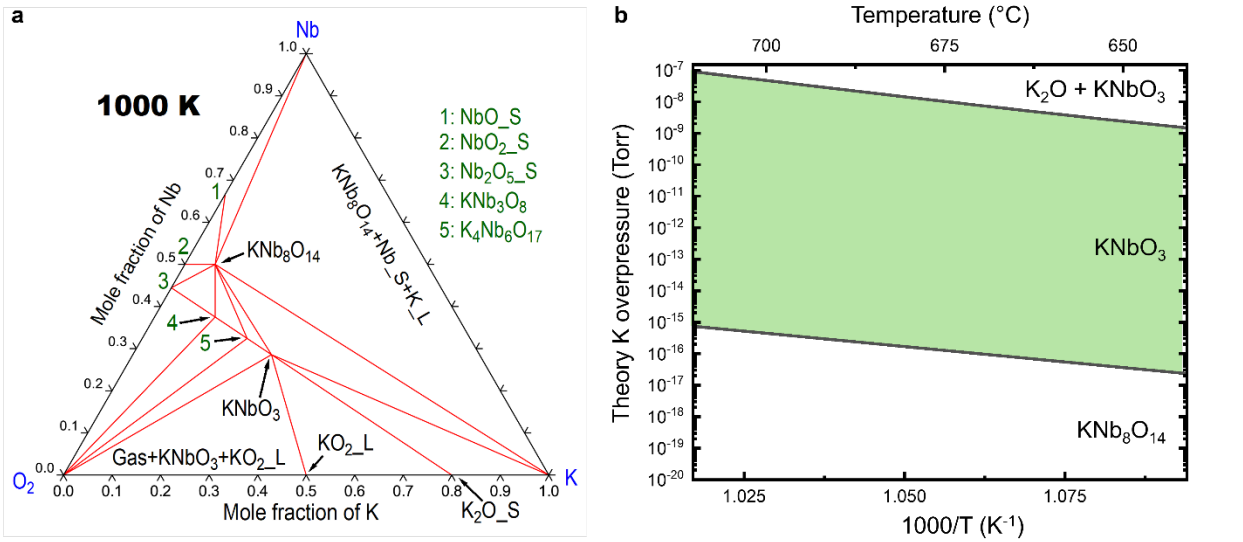



**Figure S1: a)** Calculated isothermal phase diagram of the K-Nb-$O_2$ system at 1000 K and under a total pressure of 1 atm. Solid phases are denoted with "S", liquid phases with "L", and all ternary oxides are all solids. **b)** Thermodynamically calculated potassium overpressure as a function of growth temperature showing predicted adsorption-controlled growth window for $KNbO_3$ (shaded region), bounded by potassium-rich and potassium-deficient phase conditions. Theoretically calculated potassium partial pressures required for $KNbO_3$ growth (right axis, **Figure 1a, Main Text**) are calculated by adding the predicted potassium overpressure to the potassium partial pressure corresponding to the potassium flux that is being consumed to form $KNbO_3$ (which is equal to the niobium flux used for $KNbO_3$ growth).

**Note 1: Potassium partial pressure during $KNbO_3$ growth**

We derive the relation between the molecular beam flux $F_K$ in atoms $cm^{-2}s^{-1}$ of potassium and the corresponding equivalent pressure $P_K$ based on kinetic gas theory, following the treatment commonly used for molecular-beam epitaxy[1–3].

For a dilute gas, the beam density $N_K$ in number of atoms $cm^{-3}$ is related to the pressure $P_K$ by the ideal gas law,

$$N_i = \frac{P_i}{k_B T_i}, \qquad (1)$$

where $k_B$ is the Boltzmann constant and $T_K$ is the temperature of the potassium sources. The mean speed of potassium $\bar{c}_K$ is given by the Maxwell–Boltzmann distribution,

$$\bar{c}_i = \sqrt{\frac{8k_B T_i}{\pi m_i}}, \qquad (2)$$

where $m_K$ the molecular mass of potassium. In an ideal gas with isotropic velocity distribution, the potassium flux incident on a surface is $N_K \bar{c}_K/4$. In contrast, a molecular beam produced by an effusion cell consists of particles traveling predominantly in a single direction. For such a directed beam, the flux $F_K$ incident on a surface whose normal is tilted by an angle $\theta$ relative to the beam axis is

$$F_i = N_i \bar{c}_i \cos\theta. \qquad (3)$$

Here, $\theta$ is the angle between the beam propagation direction and the surface normal. For a Vecco Gen 10 MBE this angle is 40°. Substituting Eq. (1) and (2) into (3) and solving for $P_K$ gives:

$$P_i = \frac{F_i}{\cos\theta}\sqrt{\frac{\pi m_i k_B T_i}{8}} \qquad (4)$$

where

- $P_K$ is the equivalent pressure of species $i$,
- $F_K$ is the molecular beam flux (atoms $cm^{-2}\times s^{-1}$),
- $m_K$ is the particle mass,
- $T_K$ is the beam temperature,
- $\theta$ is the beam incidence angle relative to the surface normal, and
- $k_B$is the Boltzmann constant.

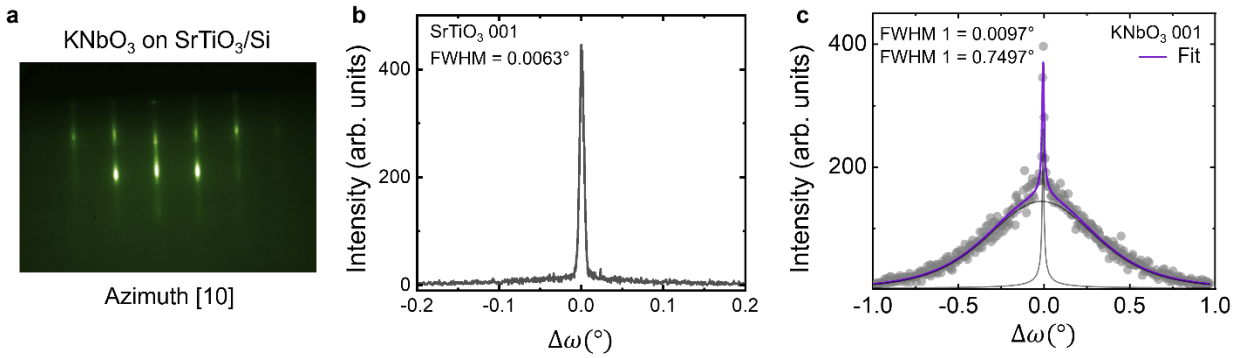



**Figure S2: a)** RHEED pattern of $KNbO_3$ grown on $SrTiO_3$/Si along the [10] azimuth direction taken post growth at the growth temperature (675 °C). **b)** X-ray rocking curve measured around $SrTiO_3$ 001 peak for the $SrTiO_3$/Si substrate. **c)** $KNbO_3$ 001 rocking curve fit with two components (modeled by Pearson VII functions, see **Note 7**) to separate the sharp central feature from the broad diffuse base, yielding FWHM = 0.0097° for the sharp component and FWHM = 0.7497° for the broad component.

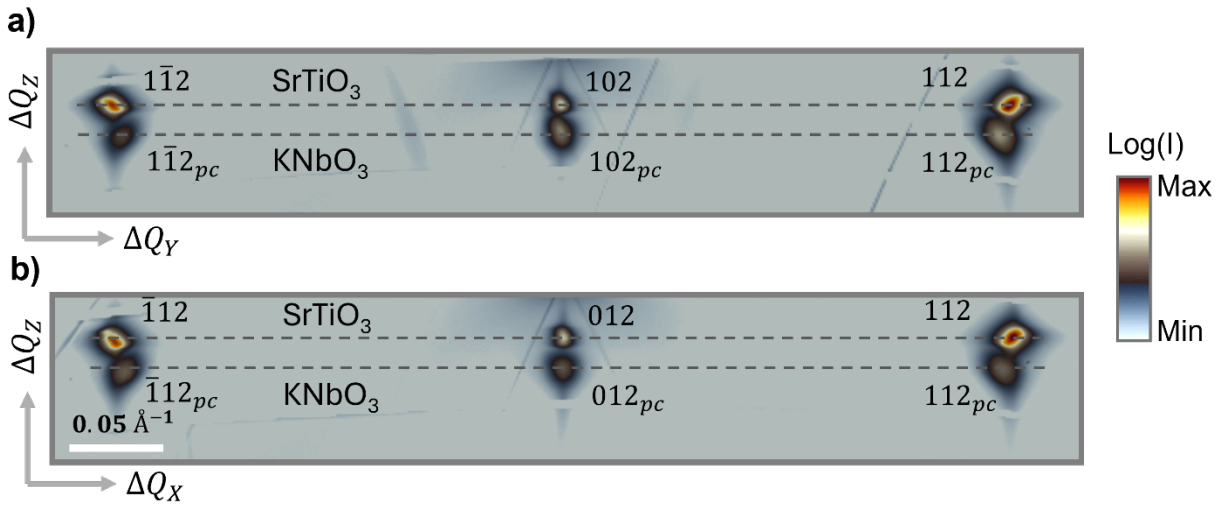



**Figure S3:** Large area reciprocal space maps (RSM) of $KNbO_3$ on $SrTiO_3$/Si along **a)** $Q_y$ and **b)** $Q_x$ reciprocal space directions showing epitaxial relationship between $KNbO_3$ and $SrTiO_3$ buffer layer.

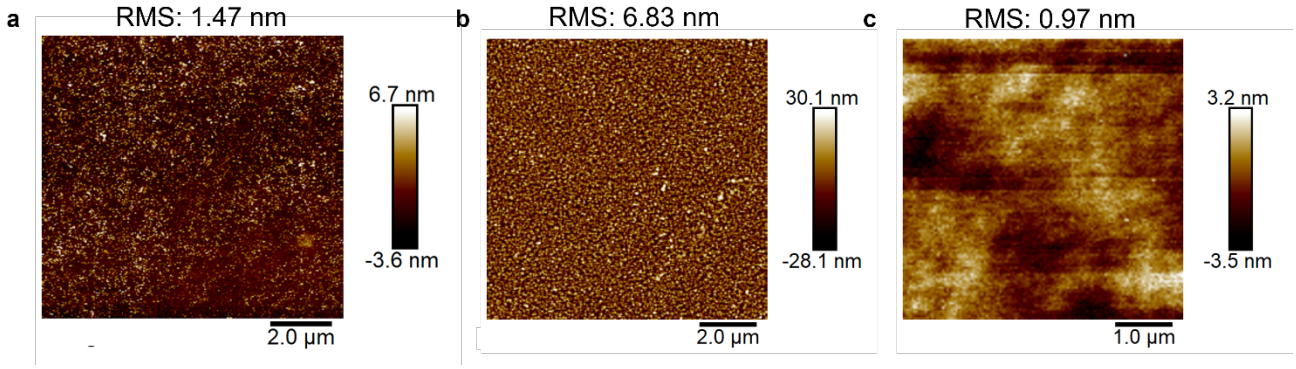



**Figure S4:** AFM maps taken over a 10 $\mu m \times 10\ \mu m$ area of the $KNbO_3$ films showing RMS surface roughness of **a)** 1.47 nm for 18 nm thick KNbO3 film and **b)** 6.83 nm for a 96 nm thick $KNbO_3$ film. **c)** AFM maps over a 5 $\mu m \times 5\ \mu m$ area of the SrTiO3 film on Si showing RMS surface roughness of 0.97 nm.

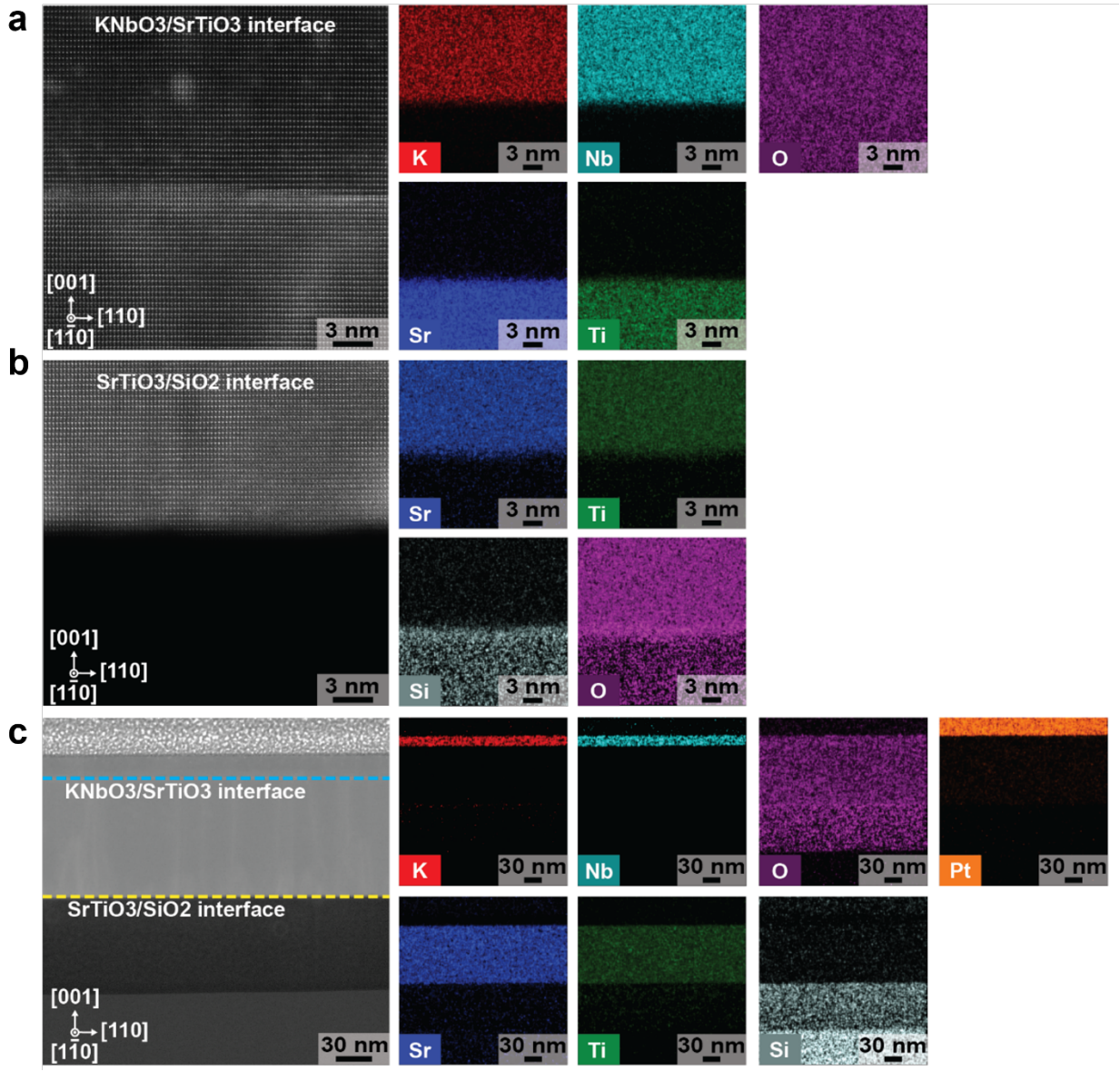



**Figure S5:** Cross-sectional scanning transmission electron microscopy (STEM) high-angle annular dark-field (HAADF) image of the $KNbO_3/SrTiO_3/Si$ stack taken at a different region of the sample. The accompanying energy-dispersive X-ray spectroscopy (EDS) elemental maps (K, Nb, Sr, Ti, O, Si, and Pt) are acquired from the same field of view and illustrate the elemental distributions across the heterostructure. The $KNbO_3/SrTiO_3$ interface **(a)**, $SrTiO_3/SiO_x$ interface **(b)** and $KNbO_3/SrTiO_3/Si$ stack **(c)** are shown.

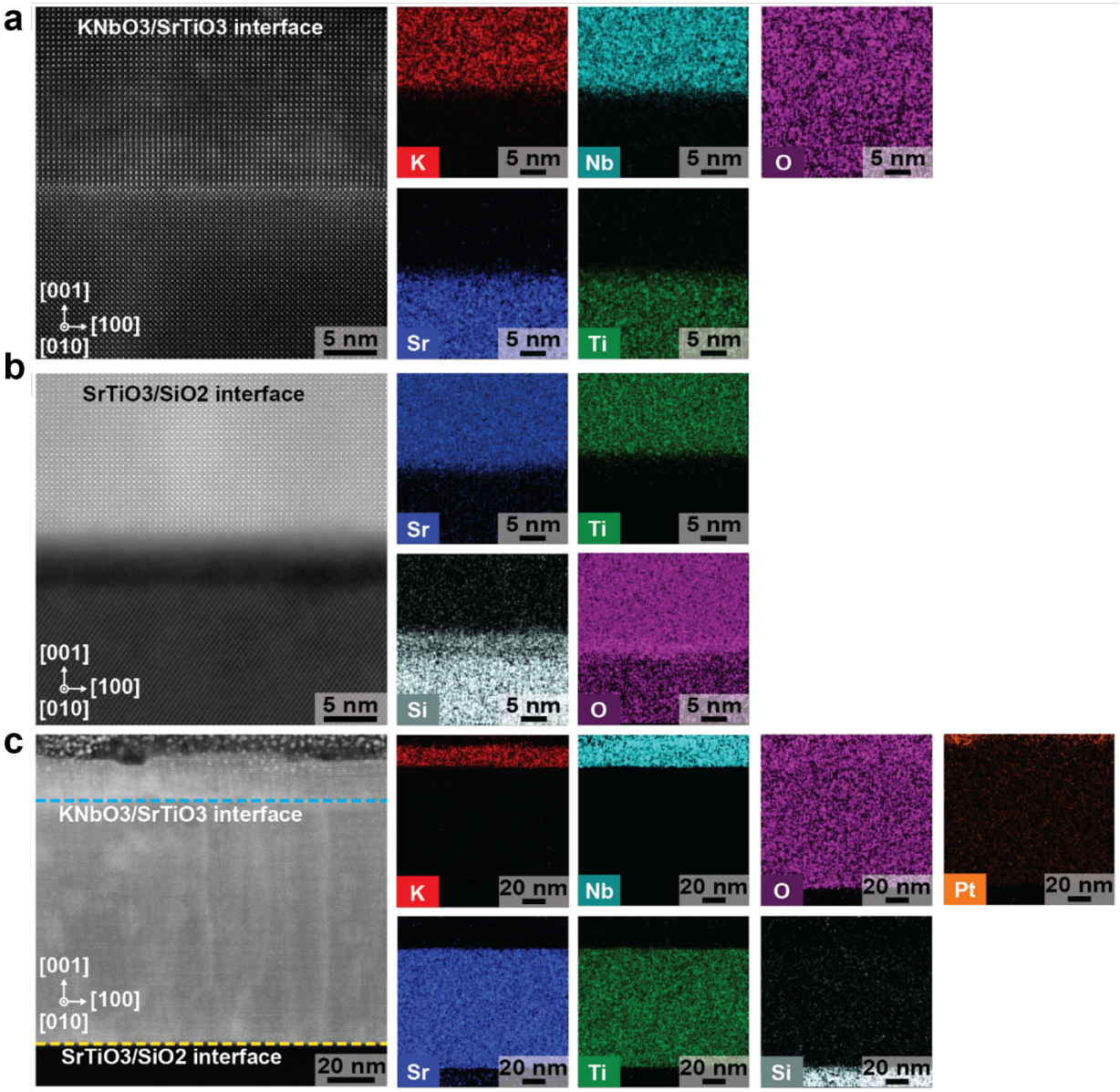



**Figure S6:** Cross-sectional scanning transmission electron microscopy (STEM) high-angle annular dark-field (HAADF) image of the $KNbO_3/SrTiO_3/Si$ stack taken at a different region of the sample. The accompanying energy-dispersive X-ray spectroscopy (EDS) elemental maps (K, Nb, Sr, Ti, O, Si, and Pt) are acquired from the same field of view and illustrate the elemental distributions across the heterostructure. The $KNbO_3/SrTiO_3$ interface **(a)**, $SrTiO_3/SiO_x$ interface **(b)** and $KNbO_3/SrTiO_3/Si$ stack **(c)** are shown.

**Note 2: Defect analysis from TEM images**

Several defect regions at the interface between $KNbO_3$ and $SrTiO_3$ and the $SrTiO_3$ buffer layer itself is highlighted in **Figure S7a**. The interface shown in this image contains local atomic steps and structurally distorted regions. There may be several possible origins of these local structural features.

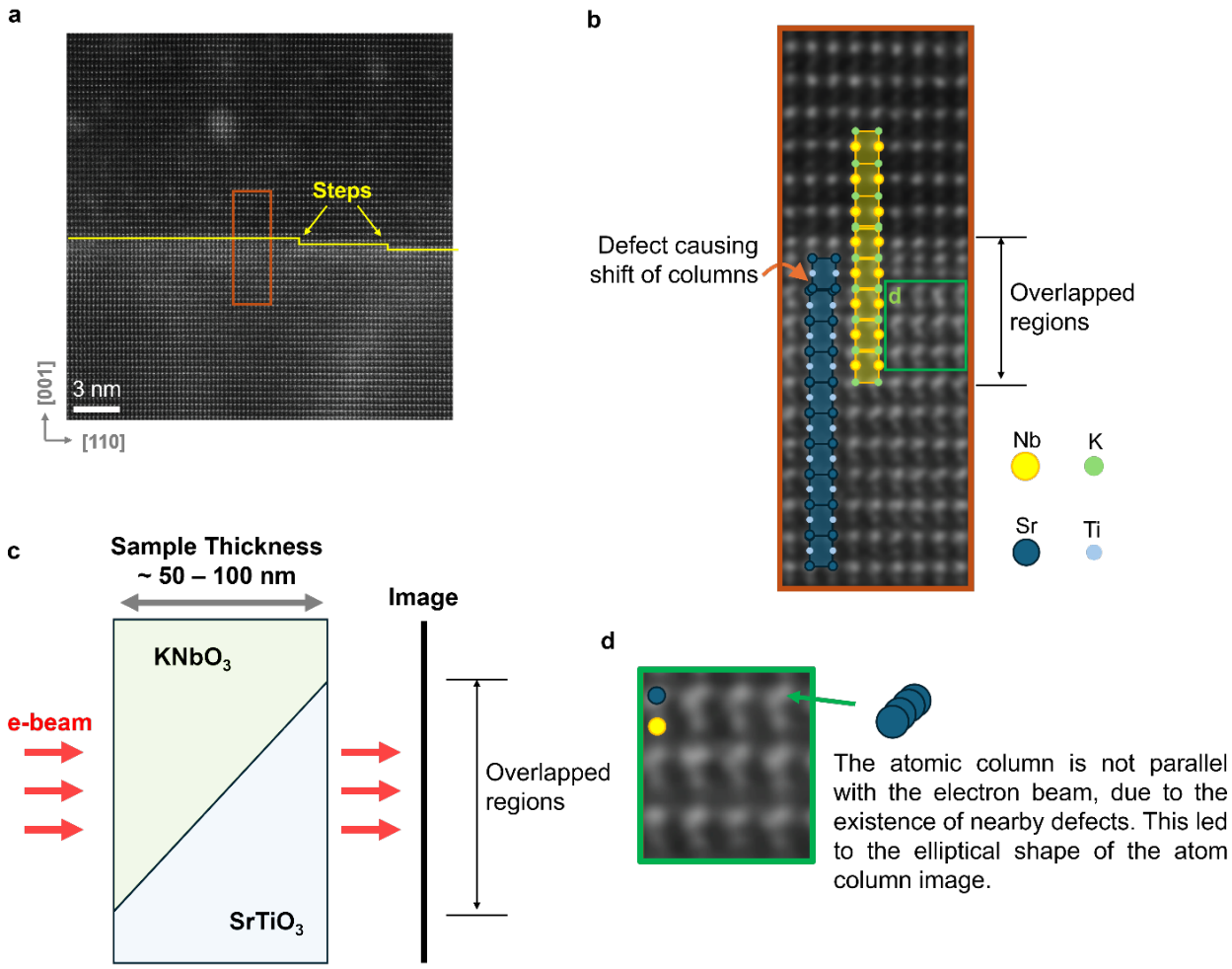



**Figure S7: a)** HAADF-STEM images of the $KNbO_3/SrTiO_3$ interface viewed along the $SrTiO_3$ $[1\bar{1}0]$ zone axis. A noticeable feature is the existence of atomic step edges at the interface, indicating that the interface is not perfectly flat. **b)** Zoomed in $KNbO_3/SrTiO_3$ interface showing two features: the $KNbO_3/SrTiO_3$ overlapped regions, and the elliptical atomic column images (green box). **c)** Schematic drawing showing the origin of the overlapped regions in (b), due to the roughness and steps at the interface and sample thickness. **d)** Enlarged illustration of the boxed region in (b), highlighting the distorted/elliptical atomic column images of Sr, suggesting that the $SrTiO_3$ may contain local defects that lead to misorientation of the crystal with respect to the electron beam direction.

First, there is a "overlapped region" at the interface, as shown in **Figure S7b**. The TEM specimen is not atomically thin; it was prepared by focused ion beam milling and has an estimated thickness of approximately 50–100 nm. Therefore, the image represents a projection of structural information through the specimen thickness (**Figure S7c**). In this case, the observed atomic steps likely indicate that the interface is not perfectly flat through the thickness direction, which is expected for a real interface. As a result,

regions near the interface may contain projected contributions from both the top and bottom layers along the electron beam direction, leading to apparent local distortions or overlapping regions in the image (**Figure S7 b-c**).

Second, the atomic structure at the interface contains local structural distortions. For example, the arrow in **Figure S7b** highlights the shift of a $SrTiO_3$ cell. For another example, **Figure S7d** shows distorted/elliptical Sr atomic column images. These structural distortions could be resulted from the following reasons.

- Lattice mismatch and strain accommodation across the interface: To examine this possibility, we performed geometric phase analysis (GPA) of the image (**Figure S8**). The GPA strain maps show that the top and bottom layers exhibit different strain states in both the in-plane and out-of-plane directions, indicating that the interface mismatch produces relative lattice offsets across the interface. When the two layers are projected together through the sample thickness, even a small relative displacement between the lattices can produce locally shifted or distorted atomic columns, which may contribute to the features observed near the interface in **Figure S7**.

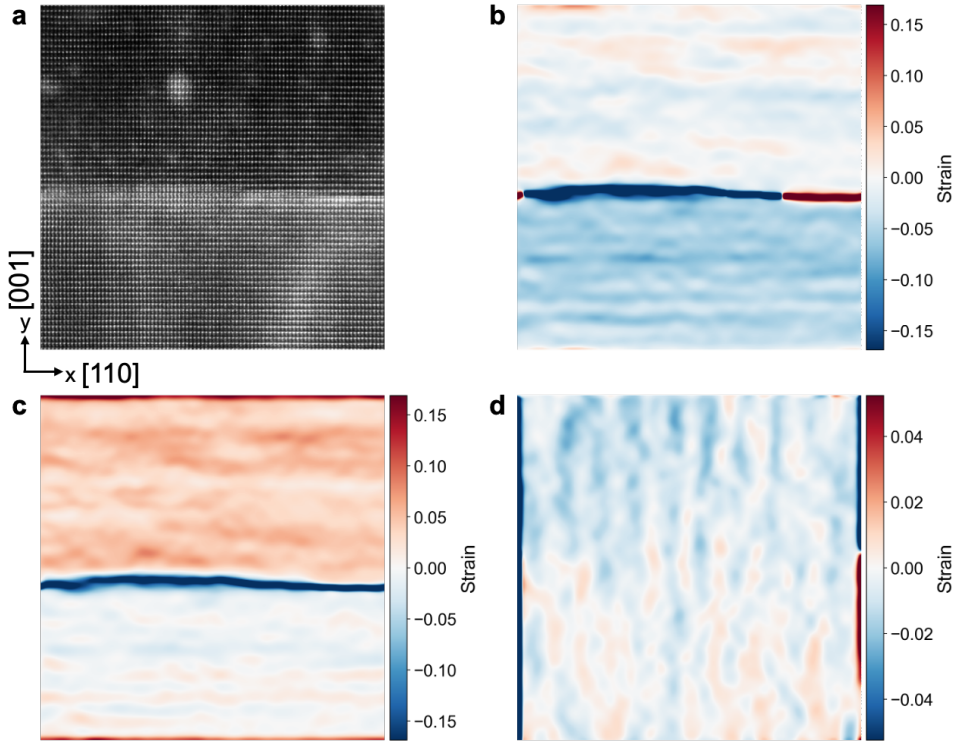



**Figure S8: a)** HAADF-STEM image of the $KNbO_3/SrTiO_3$ heterostructure after auto-cropping to a square field of view. **b)** Vertical strain map ($\varepsilon_{yy}$) computed by GPA using the $KNbO_3$ lattice as reference, showing tensile strain (red) in the $KNbO_3$ region and compressive strain (blue) in the $SrTiO_3$ region, with a locally enhanced strain at the interface exceeding that of either bulk layer. **c)** Vertical strain map ($\varepsilon_{yy}$) using the $SrTiO_3$ lattice as reference, confirming the lattice mismatch between the two materials. **d)** Horizontal strain map ($\varepsilon_{xx}$) using the $KNbO_3$ lattice as reference. Note that GPA reveals variations in the projected lattice periodicity relative to the selected reference region. Across the heterointerface, these variations may include contributions from lattice mismatch, local deformation, and changes in atomic-column contrast. The interfacial signal is therefore not assigned uniquely to elastic strain.

- Existence of planar defects: we performed fast Fourier transform (FFT) analysis of the top layer, bottom layer, and interfacial region (**Figure S9**). The FFT patterns from the top and bottom regions show similar crystalline structures. In contrast, the FFT pattern from the interfacial region contains streaking features, suggesting the possible presence of planar defects, such as stacking faults, near the interface[4]. Such defects are reasonable in this material system and may further contribute to the local structural distortion. Because the selected region is narrow and irregularly bounded, finite-window and masking effects may contribute substantially to this feature. The present FFT analysis does not uniquely identify planar defects.
- Presence of interfacial dislocations or other local defects: A previous study of similarly grown $SrTiO_3$/Si films reported threading dislocations and out-of-phase boundaries [5]. Such defects are plausible contributors to the contrast variations observed here, but their identities and densities have not been quantified in the present specimens. Defects such as interfacial dislocations, as well as possible point defects, may also contribute to the distorted contrast observed in the current cross-sectional image.

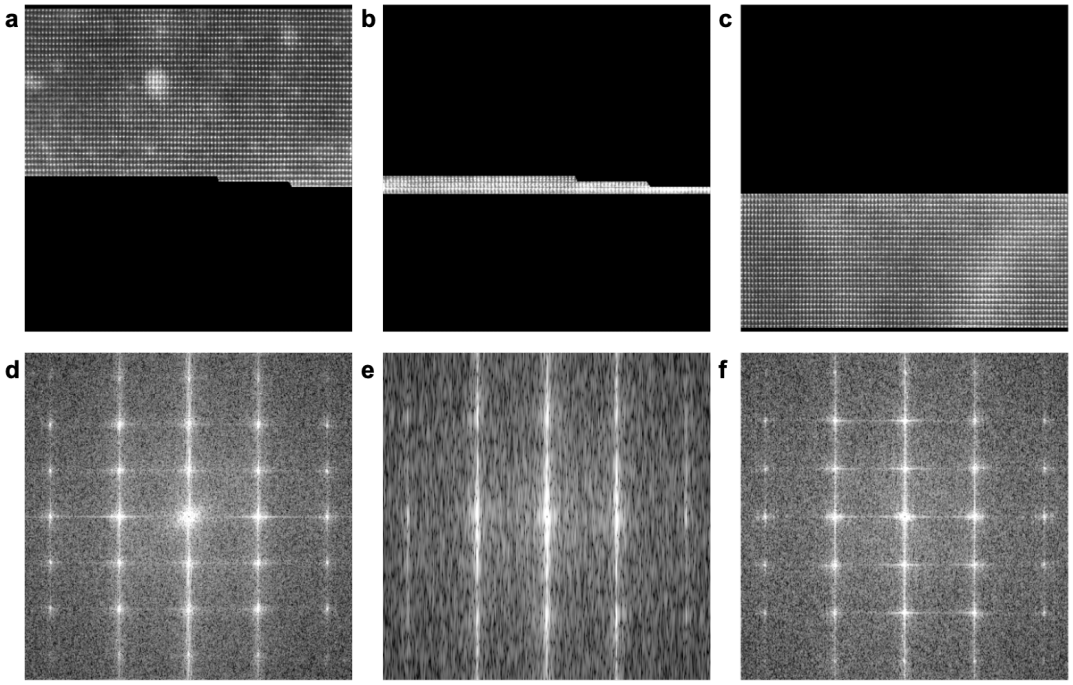



**Figure S9: a-c)** HAADF-STEM images of the $KNbO_3$ region, interface region, and $SrTiO_3$ region, respectively. Regions outside each selected area were masked prior to the FFT analysis. **d)** FFT pattern of the $KNbO_3$ region, showing a well-defined periodic spot pattern characteristic of the $KNbO_3$ lattice. **e)** FFT pattern of the interface region. **f)** FFT pattern of the $SrTiO_3$ region, showing well-defined periodic diffraction spots consistent with the $SrTiO_3$ lattice.

**Note 3: Derivation of SHG fitting equations for room temperature orthorhombic model**

**Figure 3a, Main text** shows a schematic of the SHG setup used for our experiments. For our modeling, we define a lab coordinate system $(X, Y, Z)$ that is attached to the direction of the incoming beam, with X || *p* polarization, Y || *s* polarization (**Figure 3a, Main text**). In addition, we define a lab coordinate system ($L_1 = [100]_L$, $L_2 = [010]_L$, $L_3 = [001]_L$) attached to the $SrTiO_3$ buffer layer where $L_1$ || [100], $L_2$ || [010] and $L_3$ || [001] direction of the $SrTiO_3$ substrate.

In the lab coordinate system $(X, Y, Z)$, the electric field of the incident fundamental beam can be expressed as $(E_o \cos\phi,\ E_o sin\ \phi, 0)$ where $\phi$ is the angle through which the polarization is rotated by a half wave plate as shown in **Figure 3a**. For an incidence angle $\theta$ on the sample (see **Figure 3a**), the electric field of the incident beam can be transformed to the lab coordinate system and expressed as $(E_o \cos\phi \cos\theta, E_o \sin\phi, -E_o \cos\phi \sin\theta)$.

The incident electric field induces a nonlinear polarization, $P^{2\omega}$, which can be expressed as:

$$P_i^{2\omega} \propto d_{ijk} E_j^{\omega} E_k^{\omega} \tag{5}$$

where, $d_{ijk}$ is the nonlinear susceptibility tensor and is related to the symmetry of the material under observation and $i, j, k$ are dummy subscripts related to the crystal physics direction of the material. The proportionality constant depends on incident beam fluence, Fresnel's coefficients at the film-air and film-substrate interfaces and the thickness of the films.

In crystal physics coordinates of the orthorhombic unit cell, *i* = (1, 2, 3), the nonlinear susceptibility tensor of a *mm*2 unit cell can be written in Voigt notation as:

$$d_{ij} = \begin{pmatrix} 0 & 0 & 0 & 0 & d_{15} & 0 \\ 0 & 0 & 0 & d_{24} & 0 & 0 \\ d_{31} & d_{32} & d_{33} & 0 & 0 & 0 \end{pmatrix} \tag{6}$$

We assume 8 domain variants for modelling the SHG polarimetry as shown in **Figure 3c**. For each of the domains, the relation between the crystal physics direction *i* = (1, 2, 3) and the lab coordinates are specified below

Domain 1: $[\bar{1}01]_L$ || 1, $[0\bar{1}0]_L$ || 2, $[101]_L$ || 3

Domain 2: $[\bar{1}0\bar{1}]_L$ || 1, $[010]_L$ || 2, $[10\bar{1}]_L$ || 3

Domain 3: $[101]_L$ || 1, $[010]_L$ || 2, $[\bar{1}01]_L$ || 3

Domain 4: $[10\bar{1}]_L$ || 1, $[0\bar{1}0]_L$ || 2, $[\bar{1}0\bar{1}]_L$ || 3

Domain 5: $[0\bar{1}1]_L$ || 1, $[100]_L$ || 2, $[011]_L$ || 3

Domain 6: $[0\bar{1}\bar{1}]_L$ || 1, $[\bar{1}00]_L$ || 2, $[01\bar{1}]_L$ || 3

Domain 7: $[011]_L$ || 1, $[100]_L$ || 2, $[0\bar{1}1]_L$ || 3

Domain 8: $[0\bar{1}1]_L$ || 1, $[\bar{1}00]_L$ || 2, $[0\bar{1}\bar{1}]_L$ || 3

As discussed in the main text, the 8 domain variants can be grouped into 4 pairs depending on the in-plane component of the polarization as follows:

$X+$ : Domain 1, Domain 2 (Area fraction: $A_{X+}$)

$X-$ : Domain 3, Domain 4 (Area fraction: $A_{X-}$)

$Y+$ : Domain 5, Domain 6 (Area fraction: $A_{Y+}$)

$Y-$ : Domain 7, Domain 8 (Area fraction: $A_{Y-}$)

Normal incidence ($\theta = 0°$)

Using **Equation 5**, the induced nonlinear polarization can be calculated in the lab coordinate system for each domain pair as expressed below:

| | $P_p^{2\omega}$ | $P_s^{2\omega}$ |
|---|---|---|
| Domain X+ | $d^0\cos^2\phi + d_{32}\sin^2\phi$ | $d_{24}\sin 2\phi$ |
| Domain X- | $-(d^0\cos^2\phi + d_{32}\sin^2\phi)$ | $-d_{24}\sin 2\phi$ |
| Domain Y+ | $d_{24}\sin 2\phi$ | $d^0\sin^2\phi + d_{32}\cos^2\phi$ |
| Domain Y- | $-d_{24}\sin 2\phi$ | $-(d^0\sin^2\phi + d_{32}\cos^2\phi)$ |

The net SHG intensity can be expressed as follows:

$$P_p^{2\omega} \propto \left(A^{X+}P_p^{2\omega,X+} + A^{X-}P_p^{2\omega,X-} + \left(A^{Y+}P_p^{2\omega,Y+} + A^{Y-}P_p^{2\omega,Y-}\right)e^{i\Gamma}\right)$$

where, $\Gamma = (4\pi l/\lambda)\left[n_3^{O,2\omega} - n_0^{O,2\omega}\right]$ is the phase shift generated due to the birefringence of the film. Here, $n_0^{O,2\omega} = \sqrt{2/\left[\left(1/n_1^{O,2\omega}\right)^2 + \left(1/n_2^{O,2\omega}\right)^2\right]}$, with $n_1^O$, $n_2^O$, $n_3^O$ representing the principle refractive indices of the orthorhombic unit cell and $l$ is the film thickness. The generated SHG intensity can be calculated as

$$I_p^{2\omega} = P_p^{2\omega}(P_p^{2\omega})^* = \delta A_X^2\left(P_p^{2\omega,X+}\right)^2 + \delta A_Y^2\left(P_p^{2\omega,Y+}\right)^2 + 2\delta A_x \delta A_y P_p^{2\omega,X+}P_p^{2\omega,Y+}\cos\Gamma,$$

This can be simplified to:

$$I_p^{2\omega} \propto K_{1p}\left(cos^2\,\phi + K_{2p}sin^2\,\phi\right)^2 + K_{3p}sin^2\,2\phi + K_{4p}\left(cos^2\,\phi + K_{2p}sin^2\,\phi\right)sin\,2\phi \qquad (7)$$

where,

$$K_{1p} = \delta A_X^2 d_0^2 \;\; K_{2p} = \frac{d_{32}}{d_0} \;\; K_{3p} = \delta A_Y^2 d_{24}^2 \;\; K_{4p} = 2\delta A_X \delta A_Y d_0 d_{24}\cos\Gamma$$

$d^0 = d_{15} + \frac{d_{33}+d_{31}}{2}$, $\delta A_X = A_{X+} - A_{X-}$ and $\delta A_Y = A_{Y+} - A_{Y-}$. Similar expressions can also be derived for $I_s^{2\omega}$ where the equivalent coefficients can be expressed as:

$$K_{1s} = \delta A_Y^2 d_{32}^2 \; K_{2s} = \frac{d_0}{d_{32}} \; K_{3s} = \delta A_X^2 d_{24}^2 \; K_{4s} = 2\delta A_X \delta A_Y d_{32} d_{24}\cos\Gamma$$

Similar expressions have also been shown earlier for multidomain *mm*2 model in epitaxial thin films. Normal incidence SHG polar plots of $KNbO_3$ on $SrTiO_3$/Si fitted to a multidomain orthorhombic model is shown in **Figure 3b, Main Text**.

Oblique incidence ($\theta = 45°$):

Like the normal incidence case, the oblique incidence SHG can be modeled in the same formulation and can be simplified to a similar form as **Equation 7**. The coefficients for this case can be expressed as follows:

$$K_{1p} = [(A_{X+} + A_{Y+})(2d_{31} + 2d_{33} - 4d_{15}) + A_{X-}d_{32}]^2$$

$$K_{2p} = \frac{1}{\sqrt{K_{1p}}}\left[\frac{A_{X+} + A_{Y+}}{8}(2d_{15} - 4d_{24} + d_{31} + 2d_{32} + d_{33}) + A_{X-}d_{31}\right]$$

$$K_{3p} = 2(A_{X+} - A_{Y+})^2(2d_{24} + d_{31} - d_{33})^2$$

$$K_{4p} = 2\sqrt{K_{1p}K_{3p}}\,cos\,\Gamma$$

$$K_{1s} = \frac{(A_{X+} - A_{Y+})^2}{4}(2d_{15} + d_{31} + d_{33})^2$$

$$K_{2s} = \frac{1}{4\sqrt{2K_{1s}}}(A_{X+} - A_{Y+})(2d_{32} - 2d_{15} + d_{31} + d_{33})$$

$$K_{3s} = \frac{1}{8}\left[(A_{X+} + A_{Y+})(d_{31} - d_{33}) - 2\sqrt{2}A_{Y-}d_{24}\right]^2$$

$$K_{4s} = 2\sqrt{K_{1s}K_{3s}}\cos\Gamma$$

Oblique incidence SHG polar plots fitted to a multidomain orthorhombic model is shown in **Figure S10, Supporting Information**.

**Note 4: Derivation of SHG fitting equations for high temperature tetragonal model**

Following a similar prescription, in crystal physics coordinates $i$ = (1, 2, 3), the nonlinear susceptibility tensor of a 4*mm* unit cell can be written as:

$$d_{ij} = \begin{pmatrix} 0 & 0 & 0 & 0 & d_{15} & 0 \\ 0 & 0 & 0 & d_{15} & 0 & 0 \\ d_{31} & d_{31} & d_{33} & 0 & 0 & 0 \end{pmatrix} \quad (8)$$

In this case we assume 6 domain variants for modelling the SHG polarimetry as shown in **Figure 3c**. For each of the domains, the relation between the crystal physics direction $i$ = (1, 2, 3) and the lab coordinates are specified below

Domain 1: $[010]_L \parallel 1$, $[001]_L \parallel 2$, $[100]_L \parallel 3$

Domain 2: $[0\bar{1}0]_L \parallel 1$, $[00\bar{1}]_L \parallel 2$, $[\bar{1}00]_L \parallel 3$

Domain 3: $[101]_L \parallel 1$, $[010]_L \parallel 2$, $[010]_L \parallel 3$

Domain 4: $[10\bar{1}]_L \parallel 1$, $[0\bar{1}0]_L \parallel 2$, $[0\bar{1}0]_L \parallel 3$

Domain 5: $[100]_L \parallel 1$, $[010]_L \parallel 2$, $[001]_L \parallel 3$

Domain 6: $[0\bar{1}\bar{1}]_L \parallel 1$, $[\bar{1}00]_L \parallel 2$, $[00\bar{1}]_L \parallel 3$

Unit cells with polarization direction lying in the out-of-plane direction do not contribute to an SHG response. Hence only 4 domains contribute to an SHG response as described below:

$X+$ : Domain 1(Area fraction: $A_{X+}$)

$X-$ : Domain 2 (Area fraction: $A_{X-}$)

$Y+$ : Domain 3 (Area fraction: $A_{Y+}$)

$Y-$ : Domain 4 (Area fraction: $A_{Y-}$)

Normal incidence ($\theta = 0°$)

Using Equation 1, the induced nonlinear polarization can be calculated in the lab coordinate system for each domain pair as expressed below:

| | $P_p^{2\omega}$ | $P_s^{2\omega}$ |
|---|---|---|
| Domain X+ | $d_{33}\cos^2\phi + d_{31}\sin^2\phi$ | $d_{15}\sin 2\phi$ |
| Domain X- | $-(d_{33}\cos^2\phi + d_{31}\sin^2\phi)$ | $-d_{15}\sin 2\phi$ |
| Domain Y+ | $d_{15}\sin 2\phi$ | $d_{31}\cos^2\phi + d_{33}\sin^2\phi$ |
| Domain Y- | $-d_{15}\sin 2\phi$ | $-(d_{31}\cos^2\phi + d_{33}\sin^2\phi)$ |

The net SHG intensity can be expressed as follows:

$$P_p^{2\omega} \propto \left(A^{X+}P_p^{2\omega,X+} + A^{X-}P_p^{2\omega,X-} + \left(A^{Y+}P_p^{2\omega,Y+} + A^{Y-}P_p^{2\omega,Y-}\right)e^{i\Gamma}\right)$$

where, $\Gamma = (4\pi l/\lambda)\left[n_3^{T,2\omega} - n_1^{T,2\omega}\right]$ is the phase shift generated due to the birefringence of the film, with $n_1^T$, $n_2^T$ $(= n_1^T)$, $n_3^T$ representing the principle refractive indices of the tetragonal unit cell and $l$ is the film thickness. The generated SHG intensity has the same general form as Equation 3 with the following relationship between the *K*-parameters and the nonlinear optical coefficients

$$K_{1p} = \delta A_X^2 d_{33}^2 \; K_{2p} = \frac{d_{31}}{d_{33}} \; K_{3p} = \delta A_Y^2 d_{15}^2 \; K_{4p} = 2\delta A_X \delta A_Y d_{33} d_{15} \cos\Gamma$$

$$K_{1s} = \delta A_Y^2 d_{31}^2 \; K_{2s} = \frac{d_{33}}{d_{31}} \; K_{3s} = \delta A_X^2 d_{15}^2 \; K_{4s} = 2\delta A_X \delta A_Y d_{31} d_{15} \cos\Gamma$$

where, $\delta A_X = A_{X+} - A_{X-}$ and $\delta A_Y = A_{Y+} - A_{Y-}$. Normal incidence SHG plots of $KNbO_3$ on $SrTiO_3$/Si at 600 K fitted to a multidomain tetragonal model is shown in **Figure 3b, Main Text**.

Oblique incidence ($\theta = 45°$)

Following a similar prescription fitting equations for oblique incidence polar plots can be generated. For the oblique incidence case, tetragonal unit cells with polarization in the out of plane direction also need to be considered. The derived SHG fitting equations can be expressed as the following:

$$I_p^{2\omega} = \left(\frac{\delta A_X - \delta A_Z}{8}\right)^2 [(d_{33} + d_{31} - 2d_{15})\cos^2\phi + 2d_{31}\sin^2\phi]^2$$

$$I_p^{2\omega} = \delta A_X^2 d_{31}^2 \left(\cos^2\phi + \frac{d_{33}}{d_{31}}\sin^2\phi\right)^2 + \frac{\delta A_z^2 d_{15}^2}{8}\sin^2 2\phi + \frac{\delta A_Y \delta A_z d_{31} d_{15}}{\sqrt{2}}\left(\cos^2\phi + \frac{d_{33}}{d_{31}}\sin^2\phi\right)$$

where, $\delta A_Z = A_{Z+} - A_{Z-}$. Oblique incidence SHG polar plots of $KNbO_3$ on $SrTiO_3$/Si at 600 K fitted to a multidomain tetragonal model is shown in **Figure S10, Supporting Information**.

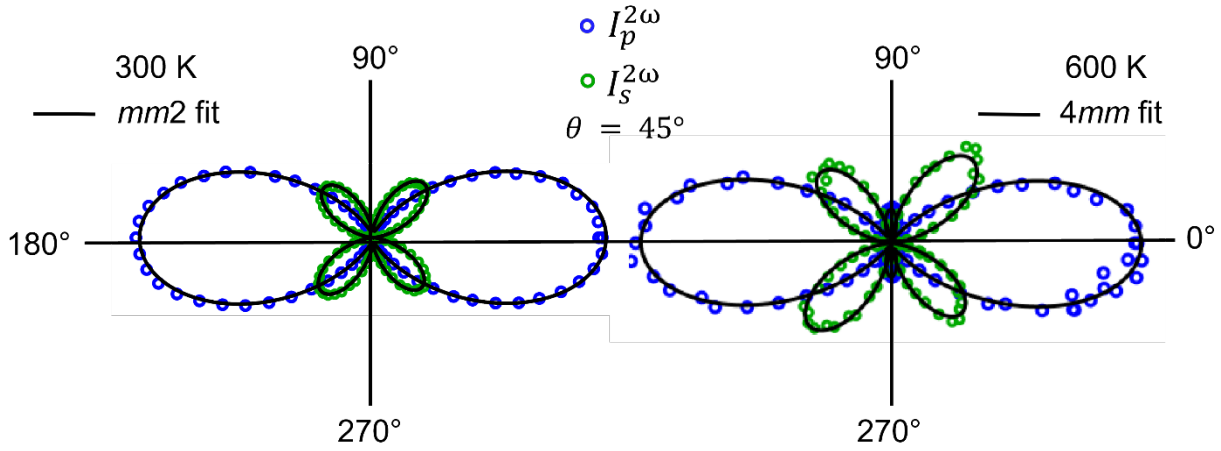



**Figure S10:** Oblique incidence ($\theta = 45°$) polarimetry of $KNbO_3$ on $SrTiO_3$/Si at 300 K (fitted to a multidomain orthorhombic model) and 600 K (fitted to a multidomain tetragonal model).

| | | | |
|---|---|---|---|
| $g_{1111}^{LL}$ | $27.8 \times 10^{-2}(m^4/C^2)$ | $p_{1111}$ | 0.5328 (Unitless) |
| $g_{1122}^{LL}$ | $-1.1 \times 10^{-2}(m^4/C^2)$ | $p_{1122}$ | 0.1584 (Unitless) |
| $g_{1212}^{LL}$ | $8.2 \times 10^{-2}(m^4/C^2)$ | $p_{1212}$ | $-0.432$ (Unitless) |
| $a_{11}$ | $a_o\left(T_s \coth\left(\frac{T_s}{T}\right) - T_s \coth\left(\frac{T_s}{T_c}\right)\right)$ | $\mu_e$ | $32.8 \times 10^{-23}\left(\frac{Kg}{m}\frac{m^4}{C^2}\right)$ |
| $T_c$ | $650K$ | $\gamma_e$ | $3 \times 10^{-9}\left(\frac{Kg}{ms}\frac{m^4}{C^2}\right)$ |
| $T_s$ | $54K$ | $B_{ij}^{e,ref}(T_0)$ | 0.2546 (Unitless) |
| $a_0$ | $3.53 \times 10^5\left(\frac{J}{m^3}\ \frac{m^4}{K\,C^2}\right)$ | $T_0$ | $398K$ |
| $a_{1111}$ | $-5.86 \times 10^8\left(\frac{J}{m^3}\ \frac{m^8}{C^4}\right)$ | $\alpha_{11}$ | $2.657 \times 10^{-5}\left(\frac{1}{K}\right)$ |
| $a_{1122}$ | $9.66 \times 10^8\left(\frac{J}{m^3}\ \frac{m^8}{C^4}\right)$ | $a_{11111111}$ | $1.74 \times 10^{10}\left(\frac{J}{m^3}\ \frac{m^{16}}{C^8}\right)$ |
| $a_{111111}$ | $2.71 \times 10^9\left(\frac{J}{m^3}\ \frac{m^{12}}{C^6}\right)$ | $a_{11111122}$ | $5.99 \times 10^9\left(\frac{J}{m^3}\ \frac{m^{16}}{C^8}\right)$ |
| $a_{111122}$ | $-2.2 \times 10^9\left(\frac{J}{m^3}\ \frac{m^{12}}{C^6}\right)$ | $a_{11112222}$ | $2.5 \times 10^{10}\left(\frac{J}{m^3}\ \frac{m^{16}}{C^8}\right)$ |
| $a_{112233}$ | $4.4 \times 10^9\left(\frac{J}{m^3}\ \frac{m^{12}}{C^6}\right)$ | $a_{11112233}$ | $-1.63 \times 10^{10}\left(\frac{J}{m^3}\ \frac{m^{16}}{C^8}\right)$ |
| $Q_{1111}$ | $0.11\left(\frac{m^4}{C^2}\right)$ | $Q_{1122}$ | $-0.053\left(\frac{m^4}{C^2}\right)$ |
| $Q_{1212}$ | $0.026\left(\frac{m^4}{C^2}\right)$ | | |

**Table S1.** Coefficients in the thermodynamic free energy function and equation of motion used for phase-field simulations[6]

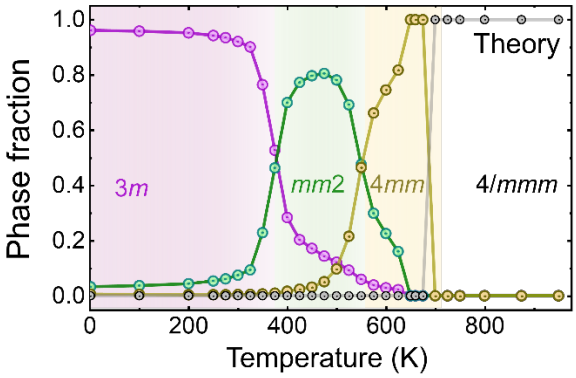



**Figure S11:** Phase-field simulated temperature evolution of phase fraction in $KNbO_3$ grown on $SrTiO_3$/Si.

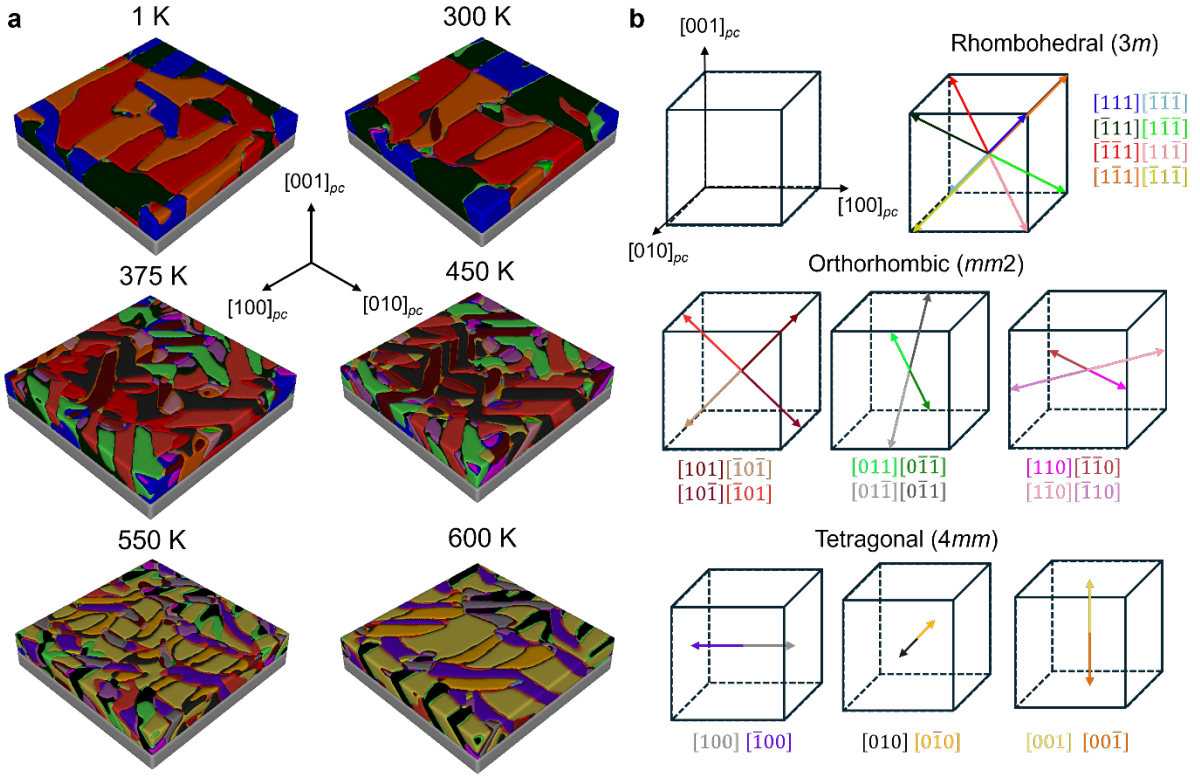



**Figure S12: a)** Phase field simulations of representative domain microstructures of strain relaxed $KNbO_3$ thin films on $SrTiO_3$/Si at various temperatures. **b)** The color code of each polarization direction corresponding to each domain variant as a legend to panel a.

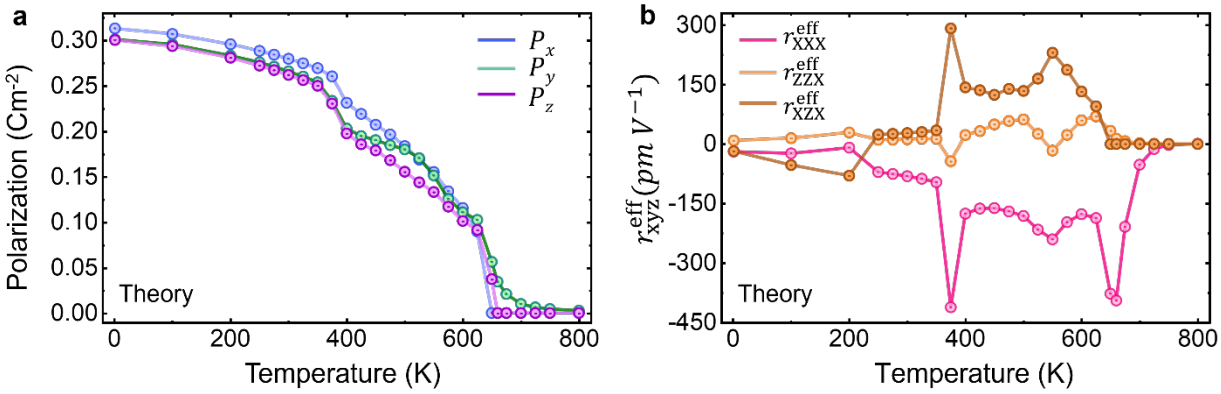



**Figure S13: a)** Phase-field predicted temperature evolution of polarization in strain relaxed $KNbO_3$ on $SrTiO_3$/Si. **b)** Phase-field predicted temperature dependence of microstructure averaged electro-optic coefficients ($r^{\mathrm{eff}}_{\mathrm{xyz}}$) of $KNbO_3$ on $SrTiO_3$/Si. Here, dummy subscripts $(x, y, z)$ refer to laboratory coordinates $(X,\ Y,\ Z)$ as shown in **Inset, Figure 5a (Main text)**.

**Note 5: PFM switching and spectroscopy**

To understand the origin of the electromechanical response, additional interferometric displacement sensing PFM (IDS-PFM) were performed. Standard optical beam deflection PFM (OBD-PFM) tracks cantilever tilt. This introduces non-local electrostatic crosstalk from the broad cantilever body. In contrast, IDS-PFM measures absolute physical displacement up down displacement of the tip directly over the tip-sample contact point. This effectively eliminates global capacitive crosstalk, while minor local electrostatic interactions can still exist at the tip-sample contact point.

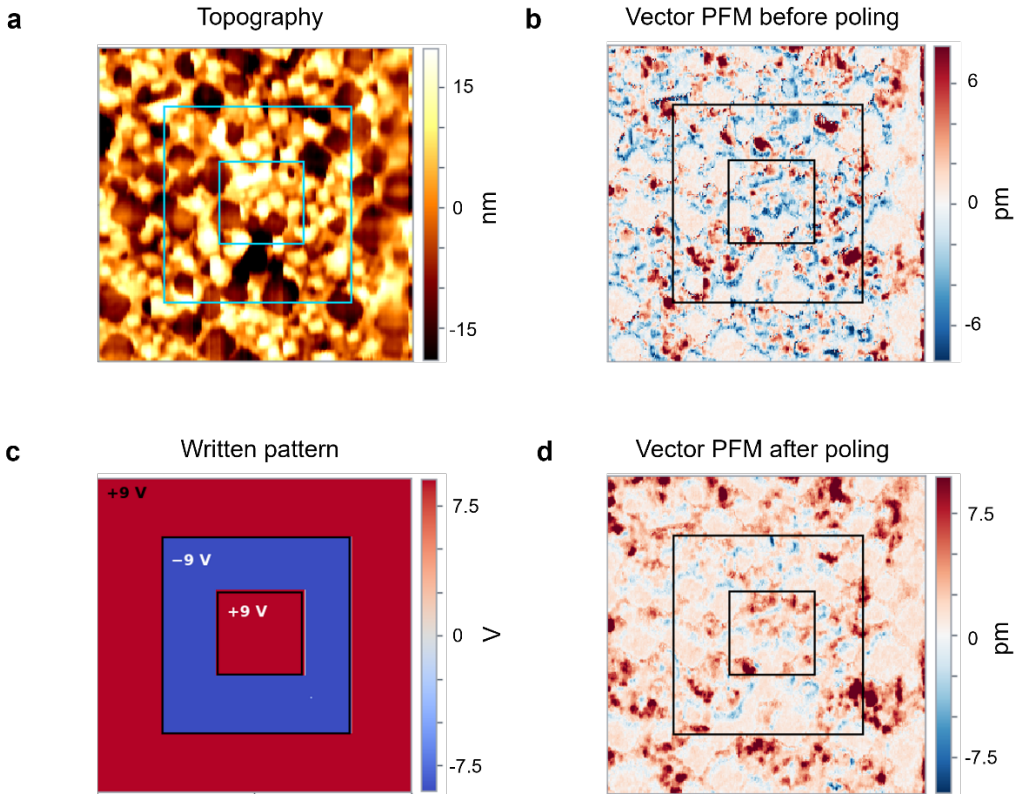



**Figure S14: a)** Topography of a 2 $\mu m \times 2\ \mu m$ region on the $KNbO_3$ film across which interferometric displacement sensing PFM (IDS-PFM) were performed. **b)** Vector PFM response ($= Acos(\phi)$, where A is the measured PFM amplitude and $\phi$ is measured phase) measured before poling. **c)** Written box-in-box voltage pattern applied for poling. **d)** Vector PFM response measured after poling.

IDS-PFM experiments were performed on a 2 $\mu m \times 2\ \mu m$ region on the $KNbO_3$ films as shown in **Figure S14a**. As shown in **Figure S14b**, a piezoelectric response can be observed across this region. The non-uniformity of the piezo-response could be related to the surface roughness of the $KNbO_3$ film. To test ferroelectric switching, a box-in-box poling experiment was performed by applying a voltage pattern as shown in **Figure S14c**. As shown in **Figure S14d**, the vector PFM response ($= Acos(\phi)$, where A is the measured PFM amplitude and $\phi$ is measured phase) after poling reveals no reversal contrast across the written voltage pattern, indicating no polarization reversal was observed. We attribute this to the absence of a bottom electrode in the $KNbO_3$ film grown on ~ 100 nm $SrTiO_3$ buffer layer on silicon.

To further characterize the local electromechanical response, switching spectroscopy PFM (SS-PFM) was performed across the film, with local hysteresis loops fitted using a nine-parameter phenomenological model[7]. From this fitting, spatially resolved maps of the switchable polarization and work of switching can be derived as shown in **Figure S15a**. Representative hysteresis loops from two different locations on the film are shown in **Figures S15b** and **S15c**. While some pixels show partial hysteretic behavior with finite switchable polarization and non-zero work of switching, no pixel yielded a clean 180° switching loop was observed across the grid. While no ferroelectric switching could be established, due to the absence of a bottom electrode, the finite switchable polarization and work of switching observed in some regions nonetheless suggest a local electromechanical response beyond pure electrostatic artifact.

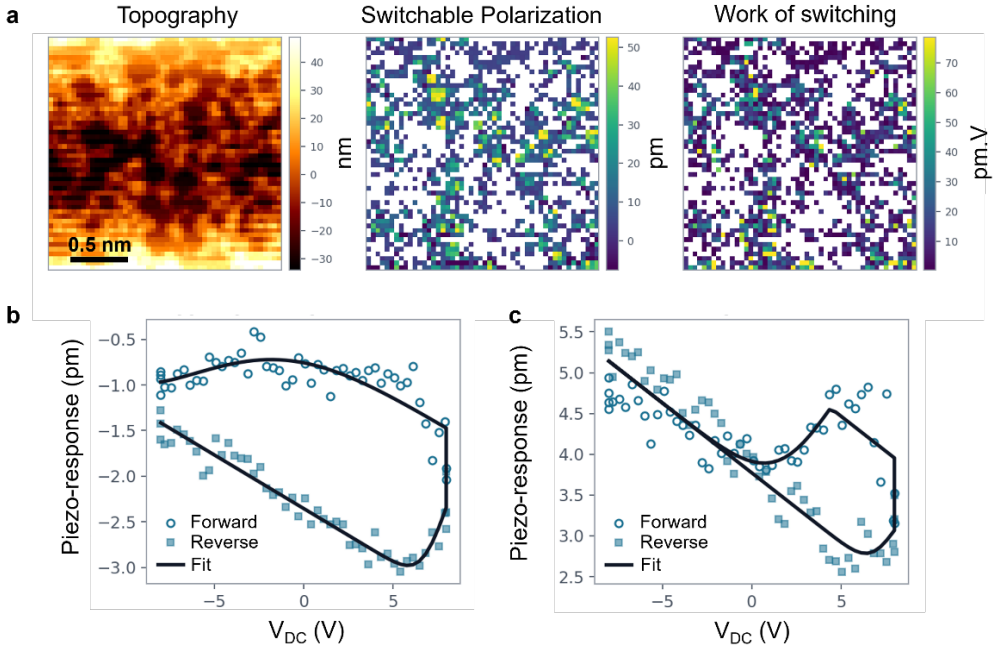



**Figure S15: a)** AFM topography and corresponding maps of the switchable polarization and work of switching. Switching spectroscopy-PFM (SS-PFM) is measured across ~5,000 points and is fitted to a nine-parameter phenomenological model. From this fitting, the switchable polarization and work of switching is derived. **b,c)** Representative PFM switching loop measured in two different positions of the sample fitted to the nine-parameter model.

To understand the PFM phase distribution, we analyze the phase as a function of signal-to-noise ratio (SNR) of the piezoelectric amplitude across the measured region (**Figure S16**). The SNR bins separate pixels by the reliability of their piezoelectric response between pixels where the signal is barely above the noise floor (SNR 0–2) and pixels with a high-confidence piezoelectric response (SNR > 10). Importantly, irrespective of the SNR bin, the phase shows a unimodal distribution with a single peak at 0° and no secondary peak at 180°. This confirms the spatially uniform phase previously observed in vertical PFM measurements.

This is consistent with the presence of a built-in electric field (imprint) in the $KNbO_3$ film, which preferentially stabilizes one polarization orientation over the other. Such built-in fields have similarly been observed in $BaTiO_3$ films grown on $SrTiO_3$/Si and can be attributed to asymmetric charge screening between the top (air) and bottom ($SrTiO_3$/Si) interfaces, or to inhomogeneous defect dipoles and surface defects. In this case, one polarization direction is favored over the other. For example, the X+ and Y+

variants could be favored over X− and Y−. The phase-field simulations, which do not include such a built-in field, show both domain orientations.

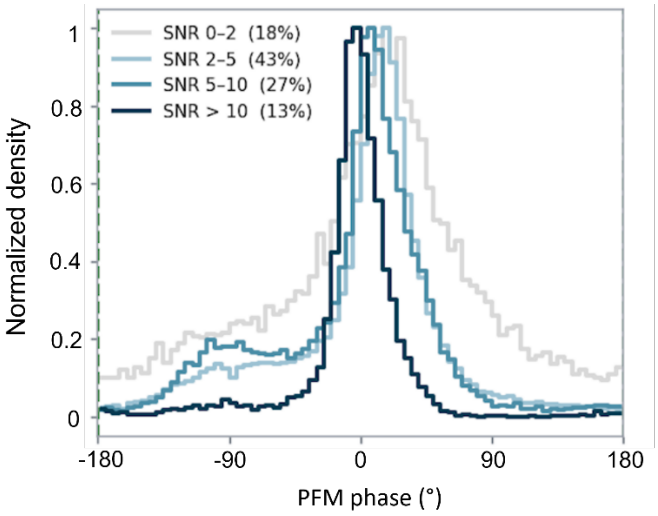



**Figure S16:** Signal-to-noise ratio (SNR)-dependent pixel density distribution of the PFM phase measured for the $KNbO_3$ film. The pixels density is binned by the SNR of the piezoelectric amplitude response (SNR 0–2: 18% of pixels; SNR 2–5: 43%; SNR 5–10: 27%; SNR > 10: 13%).

**Note 6: SHG microscopy**

The second-harmonic generation (SHG) intensity measured at polarization channel $i$ ($i = s\ or\ p$) as a function of input polarization angle $\theta$ is given by:

$$I_i^{2\omega} = K_{1i}(K_{2i}\sin^2\theta + \cos^2\theta)^2 + K_{3i}\sin^2(2\theta) + K_{4i}(K_{2i}\sin^2\theta + \cos^2\theta)\sin(2\theta)$$

where $i = p$ or $s$ depending on the measured SHG polarization. SHG intensity maps were acquired at four input polarization angles ($\theta = 0°, 45°, 90°, 135°$) for both $p$ and $s$ output channels, yielding eight $90 \times 90$ pixel spatial maps over a $15 \times 15\ \mu m^2$ area.

From the above equation, at φ = 0° and φ = 90°,

$$I_i(0°) = K_{1i}$$

$$I_i(90°) = K_{1i} \cdot K_{2i}^2$$

Giving,

$$K_{1i} = I_i(0°)$$

$$K_{2i} = \sqrt{\frac{I_i(90°)}{I_i(0°)}}$$

Similarly, from $\theta = 45°$ and $\theta = 135°$;

$$I_i(45°) + I_i(135°) = 2\left[K_{1i}\left(\frac{K_{2i}+1}{2}\right)^2 + K_{3i}\right]$$

$$I_i(45°) - I_i(135°) = 2K_{4i}\left(\frac{K_{2i}+1}{2}\right)$$

giving,

$$K_{3i} = \frac{I_i(45°) + I_i(135°)}{2} - I_i(0°)\left(\frac{\sqrt{I_i(90°)/I_i(0°)}+1}{2}\right)^2$$

$$K_{4i} = \frac{I_i(45°) - I_i(135°)}{\sqrt{I_i(90°)/I_i(0°)}+1}$$

All eight $K$ parameters (corresponding to $p$ or $s$ polarized SHG measured) are extracted pixel-by-pixel from the eight measured intensity maps.

From this, maps of SHG tensor coefficient ratios can be extracted as follows;

$$\frac{d_0}{d_{32}} = K_{2s} = \frac{1}{K_{2p}}$$

$$\frac{d_{24}}{d_0} = \left(\frac{K_{3s}K_{3p}}{K_{1s}K_{1p}K_{2s}^2}\right)^{1/4}$$

$$\frac{\delta A_X}{\delta A_Y} = \left(\frac{K_{3s}K_{1p}}{K_{1s}K_{3p}K_{2s}^2}\right)^{1/4}$$

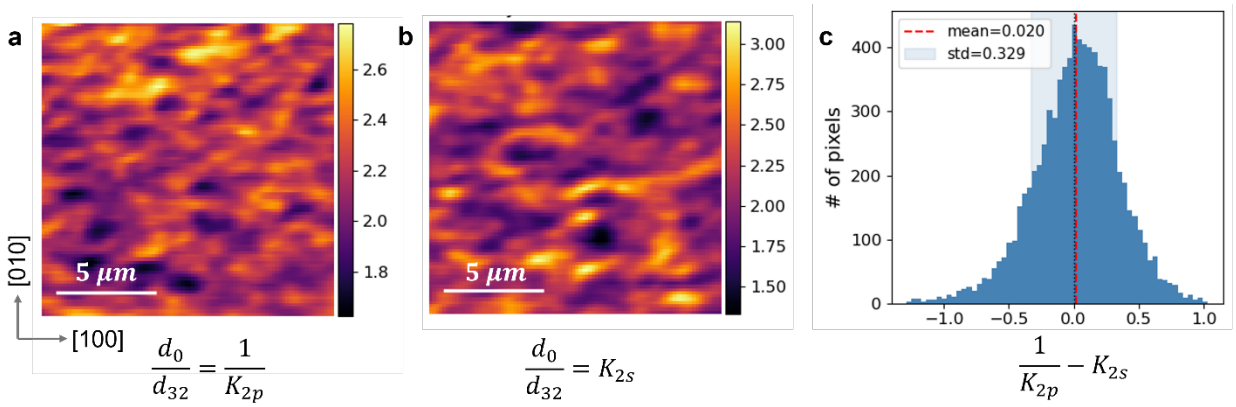



**Figure S17: a)** $d_0/d_{32}$ computed using $1/K_{2p}$. **b)** $d_0/d_{32}$ computed using $K_{2s}$. **c)** A pixel count histogram of their difference.

Each of these three ratios are computed pixel-by-pixel across the $90 \times 90$ pixel map, yielding spatially resolved images of $d_0/d_{32}, d_{24}/d_0, \delta A_X/\delta A_Y$. Since $d_0/d_{32}$ can be estimated independently from both channels ($K_{2s}$ from the $s$-channel and $1/K_{2p}$ from the $p$-channel), both estimates were computed and averaged together:

$$\left(\frac{d_0}{d_{32}}\right)_{avg} = \frac{1}{2}(K_{2s} + \frac{1}{K_{2p}})$$

**Figure S17 a - b** shows $d_0/d_{32}$ computed using the $K_{2s}$ from the $s$-channel and $1/K_{2p}$ from the $p$-channel. A pixel count histogram of their difference is shown in **Figure S17c**, showing the mean difference to be 0 with a mean of 0.02 as expected confirming the validity of the approach. **Figure S18** shows a spatial map of the $d_{24}/d_0$ ratio. The combined tensor ratio $\frac{d_{24}}{d_{32}} = \left(\frac{d_0}{d_{32}}\right)_{avg} \times \frac{d_{24}}{d_0}$ is shown in **Figure 4a,b, Main Text**.

**Figure S19** shows the correlation between $d_{24}/d_{32}$ vs. $\delta A_X/\delta A_Y$. From all 8100 pixels a Perason correlation coefficient of $-0.57$, indicating a weak spatial anticorrelation between the effective nonlinear tensor ratio and the domain population across the film.

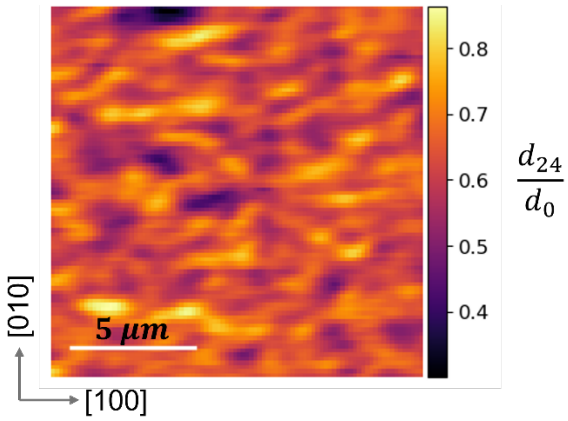



**Figure S18**: Spatial map of the $d_{24}/d_0$ ratio.

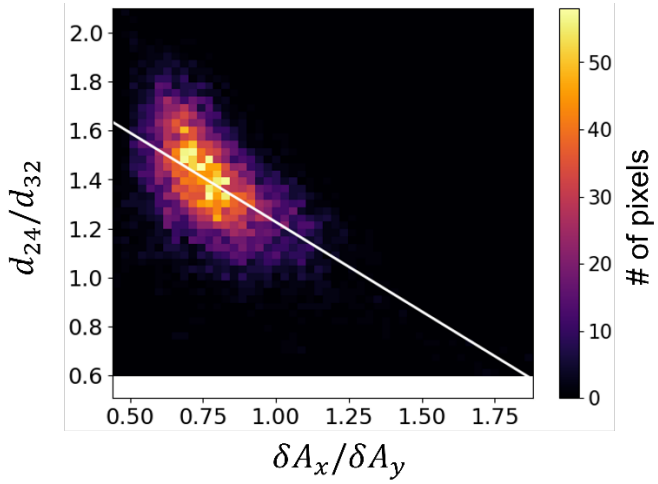



**Figure S19**: Correlation between $d_{24}/d_{32}$ vs. $\delta A_X/\delta A_Y$.

**Note 7: Temperature-dependent XRD peak fitting**

Temperature-dependent X-ray diffraction scans were collected around the $KNbO_3$ 002 film reflection and the adjacent $SrTiO_3$ (002) substrate reflection from room temperature to 700 °C. Each scan was fit using Pearson VII functions of the form

$$I(2\theta) = A\left[1 + \left(\frac{2\theta - 2\theta_0}{w}\right)^2\right]^{-m}$$

where $A$, $2\theta_0$, $w$, and $m$ represent the amplitude, peak center, width, and shape parameters, respectively, following a similar approach used previously for epitaxial $KNbO_3$ thin films grown on $SrTiO_3$ substrate[8]. At each temperature, the $SrTiO_3$ substrate peak and the $KNbO_3$ film peak(s) were fit simultaneously using a nonlinear least-squares routine, with a linear constant background term included in the model. At temperatures where the $KNbO_3$ peak resolved into two components, two Pearson VII profiles were used to capture the film contribution, sharing common width and shape parameters to avoid overfitting. Peak positions were converted to out-of-plane lattice parameters ($d$) using Bragg's law, $d = \lambda/sin(\theta)$ (for the 002 peak), with $\lambda = 1.540598$ Å (Cu $K_\alpha$).

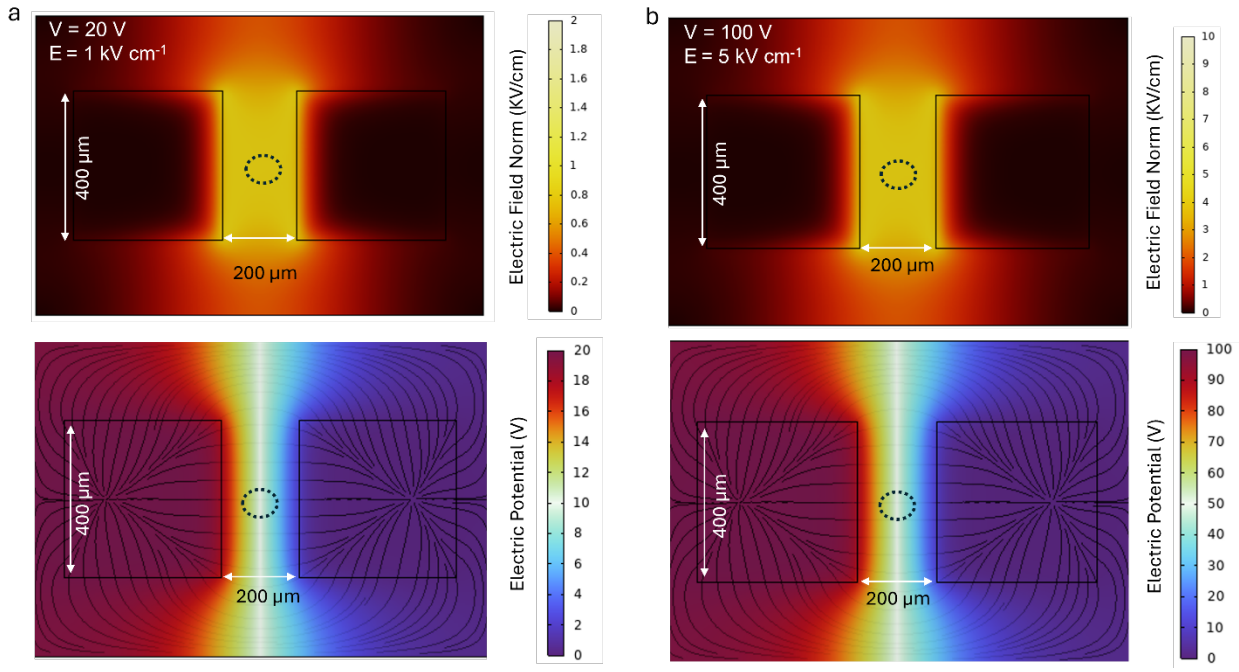



**Figure S20:** Electric field magnitude and electric potential between surface deposited electrodes as simulated in the COMSOL Multiphysics Electrostatics module for two cases. Vector field streamlines have been added to the electric potential visualization as a guide to the eye. The simulation environment consists of an 18 nm $KNbO_3$ layer on a 200 nm $SrTiO_3$ layer on top of a 200 µm Si layer. Their dielectric constants are 884[9], 200[10] and 11.7[11] respectively. Two 400 µm square surfaces are defined on the film surface, with one (right) set to ground and the other (left). The simulations are performed for two cases: **a)** Applied voltage of 20 V and **b)** applied voltage of 100 V. The COMSOL calculated electric field value in the electrode gap for both cases matches the expected value obtained when dividing the voltage applied by the electrode separation. The dotted ellipses indicate the relative full width half max diameter (~ 44.8 $\mu m$ calculated using knife-edge measurements) of the focused beam used for electro-optic characterization, projected onto the film surface at 45° incidence.

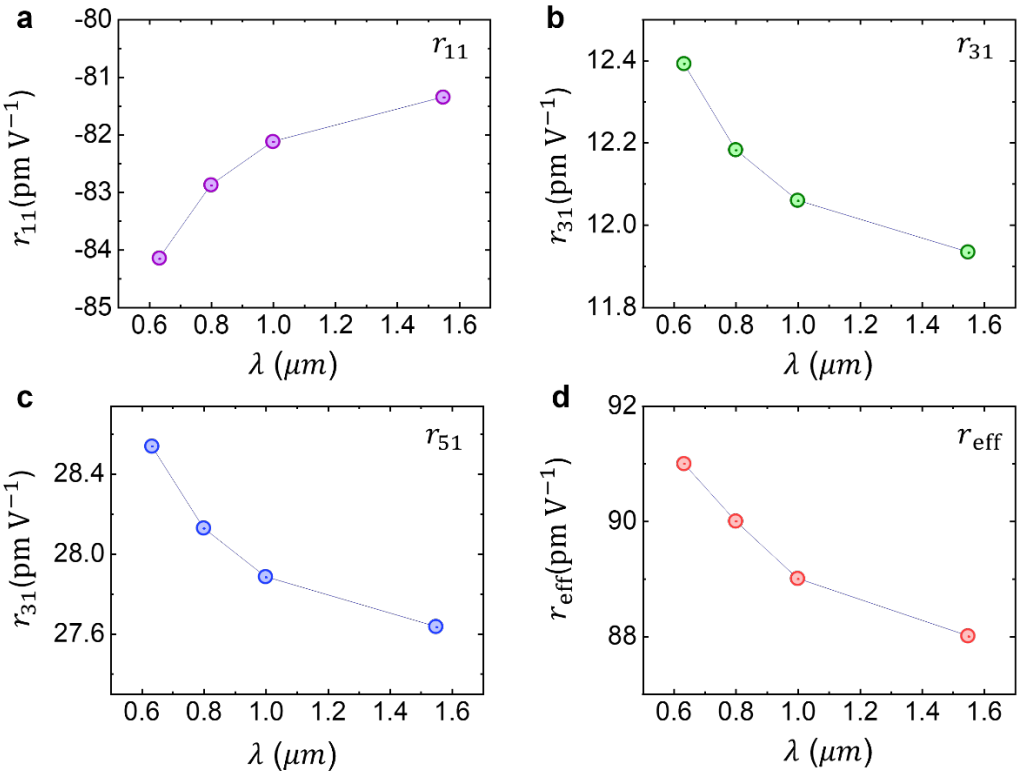



**Figure S21:** Phase-field simulated wavelength ($\lambda$) dispersion of electro-optic tensor coefficients, **a)** $r_{11}$, **b)** $r_{31}$, **c)** $r_{51}$. **d)** The simulated tensor coefficients are converted to $r_{\mathrm{eff}}$ based on experimental geometries used for measurements (see **Note 8**).

**Note 8: Refractive index and effective electro-optic coefficient ($r_{\mathrm{eff}}$) from phase-field**

**Refractive index**

The phase-field simulations yield the full electro-optic tensor coefficients $r_{11}, r_{31}$, and $r_{51}$ (in Voigt notation). In the experimental geometry, the measured quantity is an effective EO coefficient $r_{\mathrm{eff}}$ that depends on the crystal orientation, the beam propagation direction, and the applied field direction. This section describes the numerical procedure used to extract $r_{\mathrm{eff}}$ from the phase-field tensor components, implemented in Mathematica.

The zero-field dielectric susceptibility tensor $\chi_{ij}$ is obtained directly from the phase-field output. The optical indicatrix tensor $B_{ij}$ is defined as the matrix inverse of the susceptibility tensor:

$$B_{ij} = \chi_{ij}^{-1}$$

The optical ellipsoid in lab axes $(x, y, z)$ can written as:

$$B_{11}x^2 + B_{22}y^2 + B_{33}z^2 = 1.$$

The semi-axes of this ellipsoid (**Figure S22a**) give the principal refractive indices.

The eigenvalues of the cross-sectional ellipse in the plane containing the beam propagation wave vector $\vec{k}$ yields $n_o$ (ordinary) and $n_e(\theta)$ (extraordinary), where $\theta$ is the angle between $\vec{k}$ and $z$, the angle made by the propagating beam with $z$ direction.

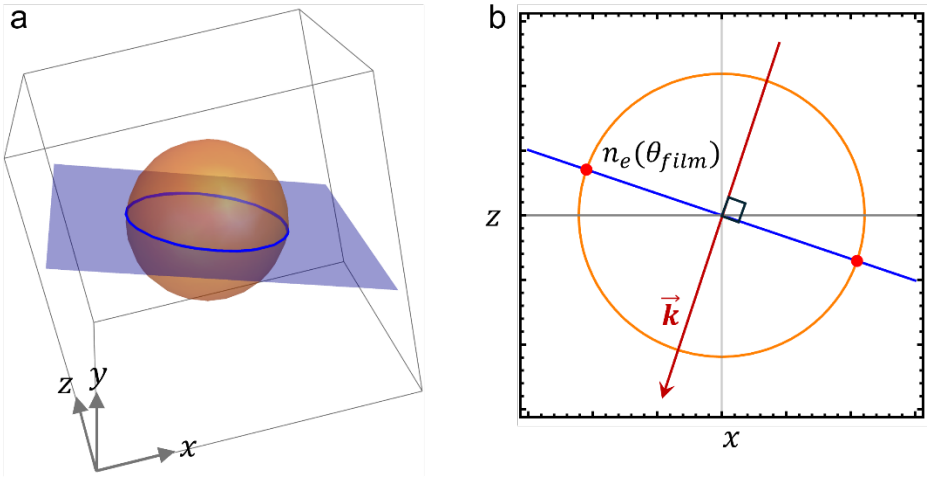



**Figure S22: a)** a) Index ellipsoid at zero field intersected by the plane normal to the propagating beam direction ($\vec{k}$). The resulting ellipse gives the semi-major axis of $n_o$ and a semi-minor axis of $n_e(\theta_{film})$. **b)** $xz$-cut of the index ellipsoid showing $n_e(\theta_{film})$ indicated by the red points.

The probe beam is incident at 45° to the sample surface normal. Applying Snell's law at the air–crystal interface,

$$\sin\theta_{film} = \frac{\sin(45°)}{n_o}$$

gives a refracted angle $\theta_{film} \approx 18.65°$ inside the material (for $n_o = 2.2117$). The refracted wave vector is

$$\vec{k} = (\sin\theta_{film}, 0, \cos\theta_{film})$$

lying in the lying in the xz-plane (**Figure S22b**). The cross-section of the indicatrix perpendicular to $\vec{\boldsymbol{k}}$ is an ellipse whose semi-axes yield $n_o$ and $n_e(\theta_{film})$.

For the phase-field susceptibility tensor at zero field ($\chi_{11} = 4.8974$, $\chi_{22} = 4.8938$, $\chi_{33} = 4.5997$, $\chi_{23} = 0.1049$, $\chi_{13} = -0.0058$ ), numerical inversion yields $n_o = 2.2117$ and $n_e(\theta_{film} = 18.65°) = 2.2065$.

**Effective electro-optic coefficient**

An electric field $E_x$ is applied along $x$. The linear EO effect modifies the indicatrix tensor by

$$\Delta B_{ij} = r_{ijk} E_k$$

For a field along *x* and the tetragonal/orthorhombic symmetry of $KNbO_3$, the non-zero increments are:

$$\Delta B_{11} = r_{111} E_1,$$
$$\Delta B_{33} = r_{331} E_1,$$
$$\Delta B_{13} = r_{131} E_1.$$

The full modified impermeability tensor $B' = B + \Delta B$ is constructed and the cross-sectional eigenvalue problem is solved again to obtain the field-modified principal indices $n_o'$ and $n_e'(\theta_{film})$.

Because the applied field $E_x$ and the wave vector $\vec{\boldsymbol{k}}$ both lie in the $xz$-plane, the ordinary polarization (along $y$) is decoupled from the electro-optic perturbation in this geometry. Consequently, $n_o' = n_o$ to first order, while only the extraordinary index changes: $\Delta n_e(\theta_{film}) \neq 0$. This is confirmed numerically in the simulation.

The effective EO coefficient is defined through the standard relation between the field-induced index change and the zero-field extraordinary index:

$$\Delta n_e(\theta_{film}) = -½\, r_{\text{eff}}\, n_e^3(\theta_{film}) E_x$$

Rearranging,

$$r_{\text{eff}} = -2\, \Delta n_e(\theta_{film}) \,/\, [n_e^3(\theta_{film})\, E_x]$$

where $\Delta n_e(\theta_{film}) = n_e(\theta_{film}) - n_e'(\theta_{film})$ and $E_x$ is the applied field magnitude. This expression directly converts the phase-field electro-optic tensor components ($r_{13}, r_{33}, r_{51}$) and the zero-field optical indicatrix into the single scalar $r_{\text{eff}}$ that is compared to the experimentally measured lock-in signal.

| Material | $r_{\text{eff}}$ $(pm\ V^{-1})$ | Thickness (nm) |
|---|---|---|
| $BaTiO_3$ on $SrTiO_3$/Si | 148 | 130 |
| $BaTiO_3$ on $SrTiO_3$/Si | 1000 | - |
| $BaTiO_3$ on $SrTiO_3$/Si | 550 | 150 |
| $BaTiO_3$ on $SrTiO_3$/Si | 140 | 78 |
| $BaTiO_3$ on $SrTiO_3$/Si | 46 | 80 |
| $BaTiO_3$ on $SrTiO_3$/Si | 119 | 100 |
| $LiNbO_3$ single crystal | 23 | - |
| $KNbO_3$ on $SrTiO_3$/Si (Expt., This work) | 113 | 18 |
| $KNbO_3$ on $SrTiO_3$/Si (Expt., This work) | 91 | 48 |
| $KNbO_3$ on $SrTiO_3$/Si (Expt., This work) | 146 | 96 |
| $KNbO_3$ on $SrTiO_3$/Si (Theory, this work) | 88 | 18 |
| $KNbO_3$ on $SrTiO_3$/Si ($\epsilon = -0.8\%$) (Theory, this work) | 900 | 18 |

**Table S2:** Tabulated film thickness and $r_{\text{eff}}$ used in **Figure 5d, Main Text**.

## References


[1] D. M. Collins, in *Pressure, Density, and Flux Formulas of Importance to Molecular Beam Epitaxy CRM-346*, Varian Associates Corporate Solid-State Laboratory Inc., Palo Alto, California, **1979**.

[2] D. G. Schlom, J. S. Harris, *"MBE Growth of High Tc Superconductors," Molecular Beam Epitaxy: Applications to Key Materials*, Edited By R.F.C. Farrow (Noyes, Park Ridge), **1995**.

[3] L. B. Loeb, *The Kinetic Theory of Gases: Being a Text and Reference Book Whose Purpose Is to Combine the Classical Deductions with Recent Experimental Advances in a Convenient Form for Student and Investigator*, 2nd Ed., Pp. 19, 106, McGraw-Hill, **1934**.

[4] Y. Yang, S. Yin, Q. Yu, Y. Zhu, J. Ding, R. Zhang, C. Ophus, M. Asta, R. O. Ritchie, A. M. Minor, *Nat. Commun.* **2024**, *15*, 1402.

[5] Z. Wang, B. H. Goodge, D. J. Baek, M. J. Zachman, X. Huang, X. Bai, C. M. Brooks, H. Paik, A. B. Mei, J. D. Brock, J.-P. Maria, L. F. Kourkoutis, D. G. Schlom, *Phys. Rev. Mater.* **2019**, *3*, 073403.

[6] A. Ross, V. Gopalan, L.-Q. Chen, *ArXiv* **2026**.

[7] N. Creange, K. P. Kelley, C. Smith, D. Sando, O. Paull, N. Valanoor, S. Somnath, S. Jesse, S. V Kalinin, R. K. Vasudevan, *Mach. Learn. Sci. Technol.* **2021**, *2*, 045002.

[8] V. Gopalan, R. Raj, *Ferroelectrics* **1997**, *200*, 343.

[9] T.-H. Lee, D.-H. Kim, B.-Y. Kim, H.-Y. Choi, J.-H. Oh, C.-Y. Kang, S. Nahm, *Acta Mater.* **2016**, *112*, 53.

[10] J. Lin, J. Cheng, P. Li, W. Chen, H. Huang, *Superlattices Microstruct.* **2019**, *130*, 168.

[11] W. C. Dunlap, R. L. Watters, *Physical Review* **1953**, *92*, 1396.